EFFECTS OF INJECTION NOZZLE CONFIGURATION

ON SECONDARY INJECTION INTO SUPERSONIC FLOW

Thesis by

Capt. Donald R. Street

United States Army

In Partial Fulfillment of the Requirements

For the Degree of

Mechanical Engineer

California Institute of Technology

Pasadena, California

1966

ACKNOWLEDGMENTS

ABSTRACT

Gaseous nitrogen and argon were injected into a primary stream of air moving at Mach 2. 56 . The gases we re injected at secondary to primary total pressure ratios from 3. 2 to 28. 6 through four different nozzles. Two nozzles, one sonic and one supersonic (M = 3. 26), injected normal to the primary stream; and two sonic nozzles injected at 45° angles to the primary flow, one injecting up-stream and the other downstream. Data consisted of static pressure measurements on the wall near the injector, total pressure profiles in the wake of the injectant plume, and concentration measurements downstream of the flow. Scale parameters were calculated based upon an analytical model of the flow field and their validity verified by experimental results. These scale heights were used to compare normalized wall side forces for the different nozzles and to compare the mixing of the two streams.

TABLE OF CONTENTS

LIST OF FIGURES

LIST OF SYMBOLS

A	area
c	discharge coefficient
C_p^*	pressure coefficient
d	injector diameter
D_o	drag/unit area
F	side force due to wall pressure
F_j	thrust of injector nozzle
F_s	total side force
h	scale height (see page 15 ff.)
K_A	mass fraction of argon
M	Mach number
$\dot{m}$	mass flow rate
P	static pressure
P_o	stagnation pressure
T_o	stagnation temperature
V	velocity
x, y, z	coordinate axes
γ	specific heat ratio
θ	angle between injectant jet and z axis

Subscripts

e	nozzle exit
j	injectant flow
t	nozzle throat
∞	mainstream flow

I. INTRODUCTION

The sonic injection of a secondary gas into a supersonic primary flow has been the subject of many studies in recent times. The disturbance in the primary flow which is caused by the injection has many current uses, including rocket thrust vector control, supersonic burning of fuel in a supersonic burning ramjet, and jet reaction control of aircraft or missiles moving through the atmosphere at supersonic speeds.

The injected fluids act as an obstruction to the flow and cause pressure fields to be set up on the wall near the injector. These pressure fields are useful in obtaining additional side forces within a rocket motor to enhance the vector control of the rocket. The injectant fluid also forms a plume as it is turned downstream and sheds vortices from both sides. These vortices accelerate the mixing of the secondary flow with the primary flow. The degree of mixing can be determined easily and can be used as a guide in the selection of optimum injection conditions to be used for supersonic burning ram jets.

This study investigated the effects of different nozzle configurations and injectant fluid pressures on the mainstream flow. Four nozzles were selected for study. The sonic nozzle (injecting normal to the mainstream flow) was used to compare results with past studies and to maintain as a standard against which to compare the results from the other nozzles. A supersonic nozzle was used which, under optimal conditions, achieved a Mach number of 3.27. The sonic and supersonic nozzles both injected normal to the mainstream flow. Two

other sonic nozzles were studied which did not inject normal to the mainstream flow. These were constructed so as to inject at an angle of 45° to the primary flow, one injecting upstream and the other in a downstream direction.

The injected gases, nitrogen and argon, were injected at pressures from 32.5 psig to 400 psig. Nitrogen was used for pressure measurements and argon was used to determine concentrations, since the thermoconductivity of argon is quite different from that of air.

Data were taken in order to determine similarity rules, a scaling factor for the disturbances, an index of the side force effects, and an idea of the mixing effectiveness of the various nozzles. The scale factors were based upon a simple, inviscid, analytical model of the flow and represent a measure of the size of the disturbance. Side forces were calculated based upon static pressure forces on the tunnel side wall. Mixing characteristics were determined by measuring the concentration of the injected gas far downstream of the nozzle. Concentrations were measured by thermoconductivity cells.

This work represents a continuation of experiments carried out by Spaid[9] and Burden[3].

II. DESCRIPTION

A. Wind Tunnel

In the performance of this experiment, use was made of the GALCIT[*] 2 × 2.5 inch supersonic wind tunnel. The tunnel was operated at a reservoir pressure of one atmosphere and at a reservoir temperature of the prevailing room temperature (usually about 76°F). Under these conditions, the tunnel has a nominal operating capacity of Mach 2.5. At normal room temperature, the Reynolds number per inch is about 5×10^{-5}. A detailed description of the construction and operation of the tunnel can be found in Reference 8.

The tunnel can be operated either closed cycle or open cycle, with or without an activated alumina dryer. Since condensation was not a problem for this experiment, the tunnel was operated with normal, undried air. During the injection of argon for the concentration measurements, the tunnel was operated open cycle. This meant that the air which had passed through the test section, and hence contained a large concentration of argon, was being vented to the air one floor below the location of the wind tunnel test section and air intake. Periodic background sampling ensured that the argon was not being recirculated, nor was it infiltrating the system.

Under the above operating conditions, the boundary layer is normally laminar. However, during the majority of the experiments, a thin strip of plastic electrical tape was placed on the tunnel wall just downstream of the throat. This tape served as a boundary layer

[*] Graduate Aeronautical Laboratories, California Institute of Technology.

trip and caused the boundary layer in the test section to become tur-
bulent without measurably affecting any other tunnel operating charac-
teristics. A laminar boundary layer was restored by removing the
tape and cleaning the nozzle with acetone. Boundary layer surveys
and schlieren photographs (see Figure 2) revealed that the turbulent
boundary layer was on the order of 0. 2 inches thick. The laminar
boundary layer (see Figure 5) was found to be slightly less than 0. 1
inches thick.

In Figures 2 through 6, a small shock wave can be seen in
front of the bow shock and injectant plume. This shock wave was
caused by the small space between the test section block and the noz-
zle blocks. This small space was due to the insertion of an "O" ring
between the blocks to prevent leakage. The wave is so weak that it
may be considered as a Mach line. It is almost completely overcome
by the bow shock and does not measurably affect results.

B.   Coordinate System

The coordinate system used for reference purposes is an
orthogonal system, whose origin is the center of the injector nozzle.
The positive x direction is the direction of the mainstream flow. The
y direction is normal to the mainstream flow, but in the plane of the
tunnel side wall face. The z direction is normal to the side wall
face, positive in the direction of the normal injected flow.

C.   Test Block and Nozzles

The test block was machined from brass and instrumented

with 62 static pressure taps.   These taps were made from 0.031 inch
outer-diameter stainless steel tubing imbedded in the brass block.
The inner diameter of these static pressure taps was 0.020 inches.
The injection port itself was a 1/8 inch hole threaded to about 0.1
inch from the face of the test block.   This left a space for the inser-
tion of an "O" ring between the block and the nozzles when the nozzles
were inserted into the hole.   The 62 taps were aligned in rows and
columns across the face of the block (see Table I for the x and y co-
ordinates of the pressure taps).

The sonic nozzle was machined from stainless steel.   The
main section of tubing was drilled to 1/8 inch inner diameter.   Be-
tween this tube and the nozzle itself was a short, straight section of
7/64 inch inner diameter tubing from which the nozzle converged to
the orifice which was 3/64 inch in diameter.   The nozzle half angle
was 14°.   The outer configuration was exactly like that of the 45°
angle nozzles (see Figure 1).

The supersonic nozzle had the same dimensions as the sonic
nozzle up to the throat.   But, from the throat, it expanded back to
7/64 inch diameter through another 14° half angle cone.   It was con-
structed of brass, as were the 45° angle nozzles.

The ports for the 45° angles were drilled at exactly 45°.
However, the flow passing through the nozzles did not turn through a
complete 45° angle.   Measurements with the schlieren system with
no tunnel flow showed that the angle was 34° (from a line normal to
the test block face).   This fact was taken into account for scale height
and thrust computations.

TABLE I

Wall Static Pressure Tap Coordinates

Expressed in Inches

No.	X	Y	No.	X	Y
0	-0.50	0	29	0	-0.25
1	-0.375	0	30	0	0.125
2	-0.25	0	31	0	0.25
3	-0.1875	0	32	0	0.375
4	-0.125	0	33	0	0.50
5	0.125	0	34	0.125	0.25
6	0.25	0	35	0.125	0.375
7	0.375	0	36	0.125	0.50
8	0.50	0	37	0.125	0.625
9	0.625	0	38	0.25	0.25
10	0.75	0	39	0.25	0.50
11	0.875	0	40	0.25	0.625
12	1.00	0	41	0.25	0.75
13	1.125	0	42	0.375	-0.50
14	1.25	0	43	0.375	0.25
15	1.375	0	44	0.375	0.50
16	1.50	0	45	0.375	0.625
17	1.625	0	46	0.375	0.75
18	1.75	0	47	0.375	0.875
19	1.875	0	48	0.375	1.00
20	-0.25	0.125	49	0.625	0.25
21	-0.25	0.375	50	0.625	0.50
22	-0.1875	0.0625	51	0.625	0.75
23	-0.125	-0.125	52	0.625	0.875
24	-0.125	0.125	53	0.625	1.00
25	-0.125	0.25	54	0.875	-0.50
26	-0.125	0.375	55	0.875	-1.00
27	-0.0625	0.1875	56	0.875	0.25
28	-0.0625	0.3125	57	0.875	0.50

TABLE I (Continued)

No.	X	Y
58	0.875	0.875
59	0.875	1.00
60	1.375	0.50
61	1.875	0.50

D.   Injection Apparatus

The gas used for injection was drawn from standard Linde commercial cylinders, throttled through a regulator and led to the injection nozzle through 1/4 inch copper tubing.   The pressure regulator was capable of operating pressures from 0 to 600 psig.   Due to high line losses, however, the highest pressure attainable at the injection nozzle was 400 psig.   Injection pressure was measured by a static pressure tap located as close as practicable to the nozzle orifice, a distance of about 3 inches.   A Bourdon-Helix gauge of 1/4 per cent accuracy was used to measure this pressure.   The line losses from the pressure tap to the orifice were considered negligible since the diameter of the straight tube from the pressure tap to the nozzle was large compared to the diameter of the throat of the nozzle.

By a slight rearrangement of the apparatus, it was possible to include a flow meter in the line.   The flow meter was used to experimentally obtain discharge coefficients for the nozzles.   This was done by computing a theoretical mass discharge rate and dividing that into the actual mass discharge rate as measured by the flow meter.

E.   Probes

Three probes were used in obtaining the data for the experiment.   Total pressure for the profiles (Figures 10 - 13) was measured by a flat probe, ground to about 0.006 inch thick by 0.087 inch wide with an orifice 0.001 inch high.

Concentration contours and total pressure contours (Figures 14 - 18) were drawn using data from two four-pronged probes.   Both

probes were constructed from stainless steel hypodermic tubing, 0.032 inch outer diameter and 0.020 inch inner diameter. The apertures were circular and spaced 1/16 inch apart. One probe was made so that the first prong was over the injection orifice and the last prong was 3/16 inch from it in the y direction. The other probe was formed with the first prong 3/16 inch from the orifice center and the last was 3/8 inch off center. This allowed for an overlap in data gathering to help coordinate the data from each of the probes.

F. Thermoconductivity Cells

Concentrations were measured by means of a Gow-Mac thermoconductivity cell. For a complete description of the cell and its principle of operation, the reader is referred to Daynes[5] and Kingsland[6]. A short description will be given here.

The Gow-Mac thermoconductivity cell consists of four chambers into each of which a filament of fine wire is placed. These wires are connected to form a Wheatstone bridge.

Into two of the four chambers, a known reference gas such as nitrogen is introduced. When the remaining two chambers are filled with nitrogen, and a current is passed through the bridge, it will be in balance electrically. When a different sample of gas is introduced into the two remaining chambers, the thermal conductivity of the medium surrounding the two wires in these chambers changes. This causes a change in the temperature of the wires, followed by a subsequent change in their resistance. If the current through the bridge is held constant, the bridge will become unbalanced due to the resulting

change in potential across two of its four branches. The degree of imbalance can be determined by measuring the potential across the center of the bridge. If the sample which has been introduced into the sample chambers is a known binary mixture of two gases, then the voltage change can be associated with a given concentration of one gas in the other.

In order to calibrate the cells, it was necessary to prepare known mixtures of argon in air. Kingsland[6] has shown that a very satisfactory mixture can be obtained by throttling air and argon into an evacuated cylinder. By measuring their partial pressures and correcting for molecular weight differences, it is possible to calculate the mass fraction of argon in air for the sample. In this case, the correction formula is:

$$K_A = \frac{1}{1 + 0.7 \frac{P_{air}}{P_{arg}}} \ , \tag{1}$$

where

K_A = mass fraction of argon in the sample,

P_{air} = partial pressure of air in the sample,

P_{arg} = partial pressure of argon in the sample.

Since thermal conductivity is a function of pressure as well as temperature and the medium itself, the calibration must also correct for pressure differences. To do this, the bridge was balanced by placing nitrogen at one atmosphere in all four chambers and adjusting a voltage divider so that the potential across the bridge center was zero. Throughout the remainder of the calibration, as well as the

data gathering, nitrogen at one atmosphere was maintained in the reference cells. Then the sample chambers were evacuated to below 50 microns pressure and small amounts of sample gas were bled into the sample chambers after the vacuum pump was sealed off. The pressure of the sample and the potential across the center of the bridge were recorded after each addition of the sample mixture until a pressure of one atmosphere was reached.

In this manner, two curves were obtained; a curve of potential against concentration for the sample gas at one atmosphere, and a curve of voltage deviation against the ratio of the sample pressure to atmospheric pressure. Thus, when an unknown sample was taken at a pressure other than one atmosphere, the voltage correction could be found and added to the potential reading from the cell. The sum of the two potentials was then used to enter the potential-concentration curve to determine the concentration.

G. Measuring Apparatus

The potential across the thermoconductivity cells was measured by means of a Wheelco potentiometer. It is capable of measuring up to 64 millivolts, and can detect voltage variations of ± 10 microvolts. It was cross-checked with a Leeds and Northrup K-2 potentiometer.

Extremely low pressures, on the order of 7 cm of mercury or less, were measured by Boller and Chivens wind-tunnel manometers. These are oil silicon manometers which compare unknown pressures against a reference chamber which is kept at very low pressures.

For this experiment, the chamber was kept at less than 10 microns as measured by a Stokes-McCleod gauge, with a liquid-nitrogen cold trap on the line. This reference value was equivalent to about 0.1 mm of silicon oil, which was lower than the sensitivity of the manometer and hence could be considered zero.

Higher pressures were measured on a standard mercury manometer bank, open to the atmosphere at one end. These manometers are graduated in millimeters and give readings within about ± 0.2 mm. Pressure in the thermoconductivity cell sample chamber was measured by a U-tube mercury manometer, graduated in tenths of inches.

H. Graphs and Figures

The purpose of this section is to discuss the experimental techniques used to obtain the data and to point out various limitations on the data. The pressure measurements for all graphs were normalized by P_∞, the free-stream static pressure. Lengths and distances were normalized by h, the scale factor. This scale factor is a measure of the flow disturbance and is calculated from an inviscid analytical model. The description of the model and the method for calculating h are left to Section III. A.

Figures 2 through 6 were taken with Polaroid film using the schlieren system which is built onto the GALCIT tunnel. The film used was Polaroid 3000 speed, type 47. Data for Figures 7, 8, and 9 were obtained by using the axial wall static-pressure taps (0 - 19 in Table I).

The total pressure profiles (Figures 10 - 13) were computed

by means of the Rayleigh pitot formula and measured pitot *total pres-*
sures.   To do this, a constant static pressure along the data line was
assumed.   The Mach number was then determined by the Rayleigh
formula; and from the Mach number, the total pressure ratio between
the pitot total pressure reading and the actual total pressure was
found from tables.

The assumption of constant static pressure near the wall is
valid, since the flow near the wall has passed through a very steep
part of the bow shock where the shock is essentially a normal shock.
The assumption is further verified by Burden[3].   However, as the
sampling point moves farther away from the wall, the static pressure
begins to rise as the mainstream flow passes through the oblique por-
tion of the bow shock.   As the distance from the tunnel wall increases,
the static pressure continues to rise as the oblique angle of the bow
shock decreases.   This fact is confirmed by the data for Figures 10 -
13, which show the calculated mainstream local total pressure actual-
ly rising to a value higher than the overall mainstream total pressure,
a condition which cannot exist.   Thus, Figures 10 - 13 are valid near
the wall, but begin to lose validity in the vicinity of $x/h = 2.0$ and de-
crease in validity as x/h increases.

The overlapping probes explained in Part F were used to
gather data for Figures 14 - 18.   As previously explained, the probes
were spaced 1/16 inch apart.   Measurements were made at intervals
of one tenth of an inch as the probes were traversed in the z direc-
tion.   In terms of the scale parameter h , the data density for these
figures can best be represented as a grid of 7 vertical lines, spaced

at a $\Delta y/h$ of 0.22 and horizontal lines spaced at a $\Delta z/h$ of 0.35 .

(These numbers are for all nozzles except the 45° downstream nozzle,

whose corresponding numbers are 0.265 and 0.445.) Each intersec-

tion of this grid represents a data point.

Separate curves were then drawn for each horizontal line

(corresponding to z/h = constant), and each vertical line (y/h = con-

stant), in order to determine the intersection of the contour lines

with the data line. These intersections were then transferred to a

graph and connected to construct the curves shown on the final figure.

The wall static-pressure contour maps (Figures 19 - 22) were

drawn using data from the static pressure taps. Due to a lack of suf-

ficient pressure taps located upstream of the injection port (the port

is represented by a small half circle at the intersection of the two

axes x/h = 0 and y/h = 0), the region upstream of the x/h = 0 axis

was drawn mostly by interpolation of data along the two axes y/h = 0

and x/h = 0 . The remaining portions of the maps were drawn based

upon numerous data points.

III. RESULTS

A. Analytical Model

In this section, the results will be presented in the following manner. First, a brief description of the analytical model as developed by Spaid[9] will be given, followed by a description of the various flow fields within the boundary layer as suggested by the wall static pressure measurements. The last part of this section will be devoted to a description of the total or gross flow as described by the total pressure profiles and contours and by the concentration contours.

The analytical model is described in detail by Spaid[9]. Basically, it is derived by assuming that the effect of the injectant plume on the mainstream flow is equivalent to that caused by a blunt, axisymmetric body. This body is best described as a quarter sphere followed by an axisymmetric half cylinder, both of whose radii are defined as "h", the scale parameter. The body is assumed to be an interface between the mainstream flow and the injectant flow, across which no mixing takes place. A momentum balance is then set up within the control volume shown on Figure A below. The boundaries for this control volume consist of the surface of the quarter sphere, the tunnel wall under the sphere, and a plane of constant x which bounds the rear of the quarter sphere. These contours are shown in Figure A.

The injected fluid is assumed to expand isentropically from P_{o_j} to P_∞, and hence attain a velocity in the x direction at station 1 which is given by:
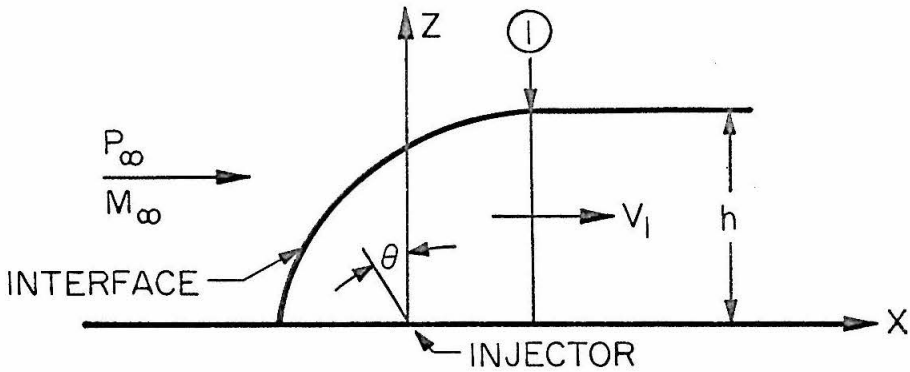
Figure A.

$$V_1 = \sqrt{(\gamma R T_{o_j})\left(\frac{2}{\gamma-1}\right)\left[1 - \left(\frac{P_\infty}{P_{o_j}}\right)^{\frac{\gamma-1}{\gamma}}\right]} \quad . \tag{2}$$

Newtonian drag on the blunt body is then equated to the change in momentum in the x direction of the injected fluid. Thus,

$$\text{Drag} = \frac{D_o \pi h^2}{2} = \dot{m}_j V_1 \quad . \tag{3}$$

When the drag is calculated, and equation (3) is solved for h, the following equation results:

$$\frac{h}{d\sqrt{c}} = \left\{ \left(\frac{1}{M_\infty}\right)\left(\frac{P_{o_j}}{P_\infty} \frac{\gamma_j}{\gamma_\infty} \frac{2}{C_p^*}\right)^{\frac{1}{2}} \times \left[\frac{2}{\gamma_j-1}\left(\frac{2}{\gamma_j+1}\right)^{\frac{(\gamma_j+1)}{(\gamma_j-1)}}\left(1 - \left\{\frac{P_\infty}{P_{o_j}}\right\}^{\frac{(\gamma_j-1)}{\gamma_j}}\right)\right]^{\frac{1}{4}} \right\} \tag{4}$$

where C_p^* is given by

$$C_p^* = \frac{2}{\gamma_\infty M_\infty^2}\left[\left(\frac{\gamma_\infty+1}{2} M_\infty^2\right)^{\frac{\gamma_\infty}{\gamma_\infty-1}}\left(\frac{\gamma_\infty+1}{2\gamma_\infty M_\infty^2-\gamma_\infty+1}\right)^{\frac{1}{\gamma_\infty-1}} - 1\right] \tag{5}$$

For the 45° angle nozzles, this derivation must be slightly modified to compensate for the fact that there will be a component of the injector velocity in the x direction. Thus, the new momentum

equation will be given by

$$\text{Drag} = \frac{D_o h^2}{\pi} = \dot{m}_j V_1 + \dot{m}_j V_{sonic} \sin\theta \tag{6}$$

where θ is measured in the positive direction as shown on Figure A. Thus, combining equations (3) and (6), we can find the correction factor to be applied to h_n (normal injection height) in order to compensate for non-normal injection, which is

$$\frac{h}{h_n} = \left[1 + \frac{V_{sonic}}{V_1} \sin\theta\right]^{\frac{1}{2}}. \tag{7}$$

This correction factor was found to be about 0.12 for the pressure ranges used in this study.

B. Flow Fields

The flow field for supersonic flow about fluid injected through a sonic nozzle was investigated in great detail by Burden[3]. His results agreed very closely with those found by this study. The following discussion will cover the case of injection through all four nozzles investigated, with turbulent boundary layers. We begin with the normal sonic nozzle discussion.

The first disturbance of the boundary layer flow comes at a distance of just over one scale factor h upstream from the orifice of the nozzle. At this point, the boundary layer meets an adverse pressure gradient created by the blockage of the flow due to the injectant plume, and the boundary layer separates. This fact is evidenced by the appearance of a separation shock (Figure 2) and a sharp pressure rise (Figures 7 and 14). The primary flow is then diverted around the region of the separated flow and thus around the orifice. A line of

maximum pressure can be seen to curve from just in front of the orifice to a distance of $x/h = 2$ behind the orifice as it goes from the bottom to the top of Figure 14. This is the intersection of the bow shock and the separation shock with the separated boundary layer and wall to form a lambda shock interaction.

The flow is diverted by a bow shock, and then begins to flow back towards the centerline, where it reattaches in the region of $x/h = 3.0$. This reattachment is evidenced by a pressure gradient in this region. The very low pressure area behind the orifice indicates a strong recirculating region.

The disturbance caused by injection through the supersonic nozzle extends upstream about as far as the sonic case, but does not extend to the side nearly as much. A brief analysis of the phenomenon will show why this would be true.

The sonic jet exits to the free stream at sonic speed, but with very high static pressure. Thus, expansion occurs laterally, since the static pressure is several orders of magnitude larger than the free stream value. Boundary layer separation occurs because the injectant plume blocks the flow some distance from the wall, and the resulting bow shock causes separation when it impinges on the boundary layer.

Flow leaves the supersonic nozzle at supersonic speeds close to Mach 3.3 with relatively low static pressure. Therefore, the predominant effect is for the injected gas, carried by the high momentum of the jet, to penetrate vertically with very little lateral expansion. The lateral expansion is much smaller than in the sonic case since

the static pressure is about 1/30 that for the corresponding sonic case. However, the boundary layer still sees an adverse pressure gradient due to blockage by the plume, and hence it separates at approximately the same point on the $x/h = 0$ axis.

As for the sonic nozzle, the supersonic nozzle seems to reattach in the vicinity of $x/h = 3.0$. This is evidenced by the strong pressure gradients in this region. Other than these two features of narrower disturbance and stronger reattachment, the sonic and supersonic boundary layer flows are very similar.

The bow shock caused by injection through the 45° downstream nozzle is very close to the orifice, as evidenced by Figures 4, 9, and 12. On the other hand, that caused by the 45° upstream nozzle is far removed from the nozzle (Figures 6, 9, and 13). This phenomenon is to be expected, since the momentum of the upstream nozzles causes a much higher pressure in front of the nozzle which keeps the bow shock detached. On the other hand, the downstream nozzle momentum reduces the pressure field, allowing the bow shock to move in closer to the orifice. Boundary layer separation occurs at about the same place for the downstream nozzle as for the sonic nozzle, again due to the obstruction caused by the injectant plume and the bow shock - boundary layer interaction.

The boundary layer separation occurs farther upstream when injection is through the upstream nozzle. The best model to explain the observed flow pattern is that of a subsonic jet impinging upon an inclined plate. The jet will divide and part of it will move in either direction along the plate (see pages 243-246, reference 10). If the

separated boundary layer is considered to act as the plate, and the injected jet has slowed to subsonic speeds, then this model can be used. In this case, that portion of the jet which is turned down towards the wall expands, causing an increased pressure field farther upstream of the nozzle. This pressure field, coupled with the advanced bow shock, causes the boundary layer to separate earlier. Further substantiation of this model can be seen from Figure 17 where the concentration of the injected gas remains large at the wall for a distance of ten injection heights downstream from the orifice. This indicates that a large portion of the flow has been turned downwards, towards the wall.

The predominant features of the mainstream or gross flow are the bow shock and the injectant plume. After the flow is diverted by the bow shock, it passes around or over the plume. The shock-induced pressure field turns the injectant flow until it is parallel to the wall. Schlieren photographs show a definite line above the injection nozzle which curves from a normal to the wall until it is almost parallel to the wall. This plume is taken to be the line of maximum penetration of the injected gas, and will be referred to as the plume height.

Examination of Figures 14 - 18 shows a kidney-shaped concentration contour for all nozzles. This indicates that vortices are shed from either side of the injectant plume. These vortices entrain the injected gases and sweep them away from the centerline, thus enhancing the mixing process.

Figures 14 - 18 reveal several other intersting features of the

mainstream flow. The most obvious feature is the depth of penetration which the various injectant gases achieve far downstream, as shown by the concentration and total pressure contours. The deepest penetration by far is caused by injection through the supersonic nozzle. This is due to the high momentum mentioned earlier. This deeper penetration suggests a different analytical model for the supersonic nozzle. This model will be discussed in paragraph III. C.

The fact that the 45° upstream nozzle gas does not penetrate into the mainstream flow as deeply as the sonic nozzle gas can be explained by reference to the jet-on-the-wall model discussed previously. Since a part of the flow is turned downward, it is obvious that the remaining flow will not have the momentum required to attain deep penetration. Also, greater mixing between the injected gas and mainstream flow can be seen by the lower concentration contours as compared to the sonic nozzle.

Comparison of Figure 18 with Figures 15 and 16 shows the effect of boundary layer state on the injection process. Spaid[9] found that whether the boundary layer was turbulent or laminar had no effect upon the injectant plume height for sonic injection. This seems to be true for the supersonic nozzle also, as Figures 15 and 18 indicate. However, the boundary layer state does seem to affect the mixing process, if not the plume height, in the case of the 45° downstream injection. Much higher concentrations in the laminar case indicate that much less mixing occurs, a phenomenon to be expected with a laminar boundary layer. The supersonic jet is not affected by the boundary layer state since it passes through the boundary layer very

quickly and mixes outside of the boundary layer. The 45° downstream jet enters the boundary layer at an angle and only at sonic speeds; thus, it remains in the boundary layer much longer and is affected by its state much more.

C. Scale Height

One of the reasons for this investigation was to determine if the scale height based on the analytical model for the sonic injection case would hold for different injection nozzle configurations. Spaid[9] originally developed the scale height to be used as a measure of the scale of the disturbance caused by injection. However, he found that this scale height agreed very closely with the measured height of the injected plume. This investigation confirmed this coincidence between computed scale height and actual injectant plume height for the sonic nozzle.

As previously mentioned, the supersonic jet penetrates farther into the mainstream flow due to its higher momentum. Figure 3 shows quite clearly that the injectant plume is at least 50 per cent higher than the sonic injectant plume (Figure 2). This suggests a new analytical model for the supersonic nozzle where the blunt body is a quarter ellipsoid with the major axis normal to the wall, followed by one half of an elliptical cylinder whose principal axes coincide with those of the quarter ellipsoid. When the derivation of the formula for h (4) is carried out for an elliptical interface, it is found to differ from the spherical model by a multiplicative constant which depends upon the eccentricity of the ellipse. Thus, for an elliptical

model with small eccentricity, h would not differ by much from the scale height for the spherical model.

The scale factor used in this experiment for all nozzles was that based on the spherical model, and Figure 8 confirms that it is still a good proportionality factor for the supersonic nozzle. In obtaining the data for this graph, injectant pressure was varied by a factor of 10, and thus h was varied by a factor of 3. Still, there was very little pressure data point deviation from a mean curve. Note that part of the observed deviation must be due to the boundary layer influence which changes as the ratio of h to boundary layer thickness changes. Therefore, even though h is not the same as the height of the injectant plume, it is still a good measure of the scale of the flow disturbance.

An attempt was made to reduce the small deviation which occurred in data points for $x/h > 0$. This was done by using the elliptical interface model and assuming that the eccentricity was a monotonically, slowly-increasing linear function of the injectant pressure. However, this assumption increased the deviation for values of $x/h < 0$. Therefore, it is believed that the spherical model scale height is the best scale parameter for the supersonic model.

Actual measurement of the plume height for the supersonic nozzle was difficult, since the plume mixed with the primary flow prior to being turned parallel to the wall. However, visual extrapolation of the visible portion of the plume in Figure 3 confirms that the penetration height must be much higher than that for the sonic nozzle.

The injection plume height for the 45° downstream nozzle is

difficult to measure for low pressures since the phenomenon occurs mostly in the boundary layer. However, for higher pressures, such as in Figure 4, the plume height was found to be about 10 per cent higher than the scale height. But, as in the case of the supersonic nozzle, the scale height seems to be a good proportionality constant, as seen in Figure 9. In this figure, the spread in the data is due to data scatter and not the disproportionate scale factors.

Measurement of the height of penetration of the 45° upstream nozzle is difficult due to the mixing process which takes place. This mixing tends to obliterate the injectant plume, as seen on the schlieren photographs (Figure 6). Where measurements were possible, the measured value is again about 10 per cent higher than the computed scale height. However, as before, the scale height h seems to be a very good scale factor, as evidenced by the lack of deviation from a mean curve seen in Figure 9.

As previously mentioned, the scale height for the sonic nozzle corresponds exactly with the plume height. Measurements were made for injectant pressures from 32.5 psig to 400 psig, and the maximum deviation found was ± 2 per cent. In several cases, the measured and computed values agreed to three significant figures.

D. Side Forces

It is of interest to determine the side forces exerted by the mainstream flow and to compare it with the force which is due to the thrust of the nozzle alone. It is this parameter which is used to determine the best nozzle to be used in rocket thrust vector control.

To determine the side force due to the mainstream flow disturbances, it is necessary to determine the pressure exerted on the wall and the area over which the pressure is acting. Since a pressure of P_∞ is acting on the undisturbed surfaces of the tunnel, we will be interested only in how the local pressures differ from P_∞ in order to determine the net wall side force. Thus, we carry out the following integral:

$$\frac{F}{P_\infty h^2} = \iint \left(\frac{P-P_\infty}{P_\infty}\right) \frac{dx}{h} \frac{dy}{h} . \tag{8}$$

This integration was carried out graphically using a planimeter and measuring the area under the curves on Figures 19 - 22. This area is then multiplied by the quantity, local pressure divided by free stream pressure, minus one $\left(\frac{P}{P_\infty} - 1\right)$. The algebraic sum of the resulting products is the normalized wall side force. The normalized wall side force is then multiplied by $P_\infty h^2$ to get the pure wall side force, independent of h. (Note: the h used for $P_\infty h^2$ must be the h corresponding to the injectant pressure used for thrust computation in equation (9) below.)

Since the theoretical exit pressure for all nozzles was of higher order magnitude than the static pressure in the wind tunnel, the nozzles were assumed to be under-expanded. Thus, the thrust of the nozzles was computed using the following formula;

$$F_j = P_{o_j} A_t \Gamma' \sqrt{\frac{2}{\gamma-1}\left[1 - \left(\frac{P_e}{P_{o_j}}\right)^{\gamma-1/\gamma}\right]} + A_e(P_e - P_\infty) \tag{9}$$

where:

A_t = nozzle throat area,

Γ' = 0.81 ,

A_e = nozzle exit area,

P_e = theoretical exit pressure based on the area ratio (A_e/A_t).

For the 45° nozzles, the thrust was multiplied by sine 56° to correct for the fact that the thrust was at an angle of 34° (see page 5).

It is realized that this method will not give a very accurate measure of the side forces for several reasons. First of all, not all of the wall area was included in the integral due to a lack of sufficient data points beyond $x/h = 3.5$ and $y/h = 3.5$. Also, as explained in II.H, the area in front of the line $x/h = 0$ was interpolated. However, this method does give an idea of the relative effects of the different nozzles.

The ratio of wall side force to thrust for the sonic nozzle was found to be 2.4. This agrees with past measurements made by many different experiments. The ratio for the supersonic nozzle was considerably lower, about 1.7. This is expected since the supersonic nozzle causes less boundary layer disturbance, and it is this boundary layer disturbance which gives the increased pressure, giving rise to the wall side forces. Also, the thrust of the supersonic nozzle is about 10 per cent higher than that of the sonic nozzle. The 45° downstream nozzle was found to be lower still, at 1.3 , again due to lesser boundary layer disturbance.

The figure for the 45° upstream nozzle was somewhat of an anomaly. It was expected that it would be higher due to the high

pressure field in front of the nozzle. However, the ratio was found to be 7. 8 , which is much higher than expected. Even though the measurements are quite crude and somewhat incomplete, it seems evident, based on these findings, that upstream injection is by far the most efficient means of attaining high side forces.

E. Mixing

The least rapid mixing between primary and secondary flows occurs in the 45° downstream, laminar boundary layer case. As far as 10 injection heights downstream from the injector, there is still a fairly large region of fluid that is more than 60 per cent injected fluid (Figure 18). The mixed region extends from the wall to a height of $z/h = 3. 0$ and to a width of just over one scale height, with the region of maximum concentration at about $z/h = 1. 5$. When the boundary layer is turbulent, the region for the 45° downstream nozzle (Figure 16) extends higher to $z/h = 3. 5$ and not as wide to $y/h = 1. 0$. The maximum concentration is only about 45 per cent and it is located just above $x/h = 2. 0$. In contrast, the most rapid mixing occurs when injecting upstream. For the 45° upstream nozzle, this mixing occurs close to the wall, centered about a line of $z/h = 1. 0$ at $x/h = 10$ (Figure 17).

The sonic nozzle and the supersonic nozzle seem to achieve about the same degree of mixing, as evidenced by Figures 14 and 15. The size of the mixing area for both is about 3h by 1.5h , though the supersonic region is slightly wider. The big difference is the location of the mixed region. At a distance of 10h from the nozzle, in the

wake of the supersonic injectant, the mixed region is centered about a line at $z/h = 2.5$, whereas the sonic nozzle mixed region at the same distance back is centered more nearly at $z/h = 1.5$. Also, all of the injected fluid is away from the wall in the supersonic wake, whereas there are trace amounts next to the wall in the sonic wake. Thus, for a supersonic burning ram jet, the supersonic nozzle would be better, since it would keep the fuel away from the walls and thus reduce heating problems.

An interesting application of the results of this experiment might be the use of nozzles to cool a surface in a supersonic stream. In this case, contrary to what one might think, the best configuration to use would be to inject upstream. Thus, the cool gases would stay close to the wall and allow greater heat transfer into the relatively cool fluid.

IV. CONCLUSIONS

The conclusions reached in this study can be summarized as follows.

1. The scale parameter, h , derived from the simple spherical model, serves as a good proportionality factor for flow disturbance for the four nozzle configurations studied.

2. The best side force effects are obtained by injecting through the 45° upstream nozzle. The others are, in order of decreasing effectiveness, sonic, supersonic, and 45° downstream nozzles.

3. The supersonic nozzle would be best for a supersonic burning ram jet, since it penetrates farther into the mainstream flow.

The study also brought out or suggested some areas for further study. One interesting nozzle configuration which could be studied is a nozzle which injects across the flow, i.e., with a component in the y direction. Another area for study would be the effect of the Mach number of the supersonic nozzle on the penetration height of the plume. Also, injection upstream through various angles should be studied in order to determine an optimum angle for wall side force effects. Finally, the shock shapes for the various nozzle configurations should be studied in order to more fully understand the phenomena accompanying secondary injection through nozzles into a primary flow.

REFERENCES

1. Ames Research Center Staff: "Equations, Tables, and Charts for Compressible Flow," NACA Report 1135, Washington, D. C. (1953).

2. Beckwith, T. G. and Buck, N. L.: Mechanical Measurements, Addison-Wesley Publishing Co., London (1961).

3. Burden, Harvey W.: "Some Effects of Secondary Injection of Gases into a Supersonic Flow," A. E. Thesis, Graduate Aeronautical Laboratories, California Institute of Technology (May, 1964).

4. Daily, C. L. and Wood, F. K.: Computation Curves for Compressible Fluid Problems, John Wiley and Sons, New York (1934).

5. Daynes, H. A.: Gas Analysis by Measurement of Thermal Conductivity, Cambridge University Press (1933).

6. Kingsland, Louis, Jr.: "Experimental Study of Helium and Argon Diffusion in the Wake of a Circular Cylinder at M = 5.8," A. E. Thesis, Graduate Aeronautical Laboratories, California Institute of Technology (June 1964).

7. Liepmann, H. W. and Roshko, A.: Elements of Gasdynamics, John Wiley and Sons, New York (1957).

8. Puckett, A. E.: "Final Report, Model Supersonic Wind Tunnel Project," Graduate Aeronautical Laboratories, California Institute of Technology, Report No. 40 (1943).

9. Spaid, Frank W.: "A Study of Secondary Injection of Gases into a Supersonic Flow," Ph. D. Thesis, Dept. of Mechanical Engineering, California Institute of Technology (May, 1964).

10. Tietjens, O. G. and Prandtl, L.: Fundamentals of Hydro- and Aeromechanics, Dover Publications, New York (1934).

$\frac{1}{8}$" MILL

.125" D.

.190" D.

45° NOZZLE

$\frac{1}{16}$" DRILL

$\frac{1}{64}$"

$\frac{1}{8}$" D.

-31-

.055

$\frac{1}{32}$ DRILL

@ 45°
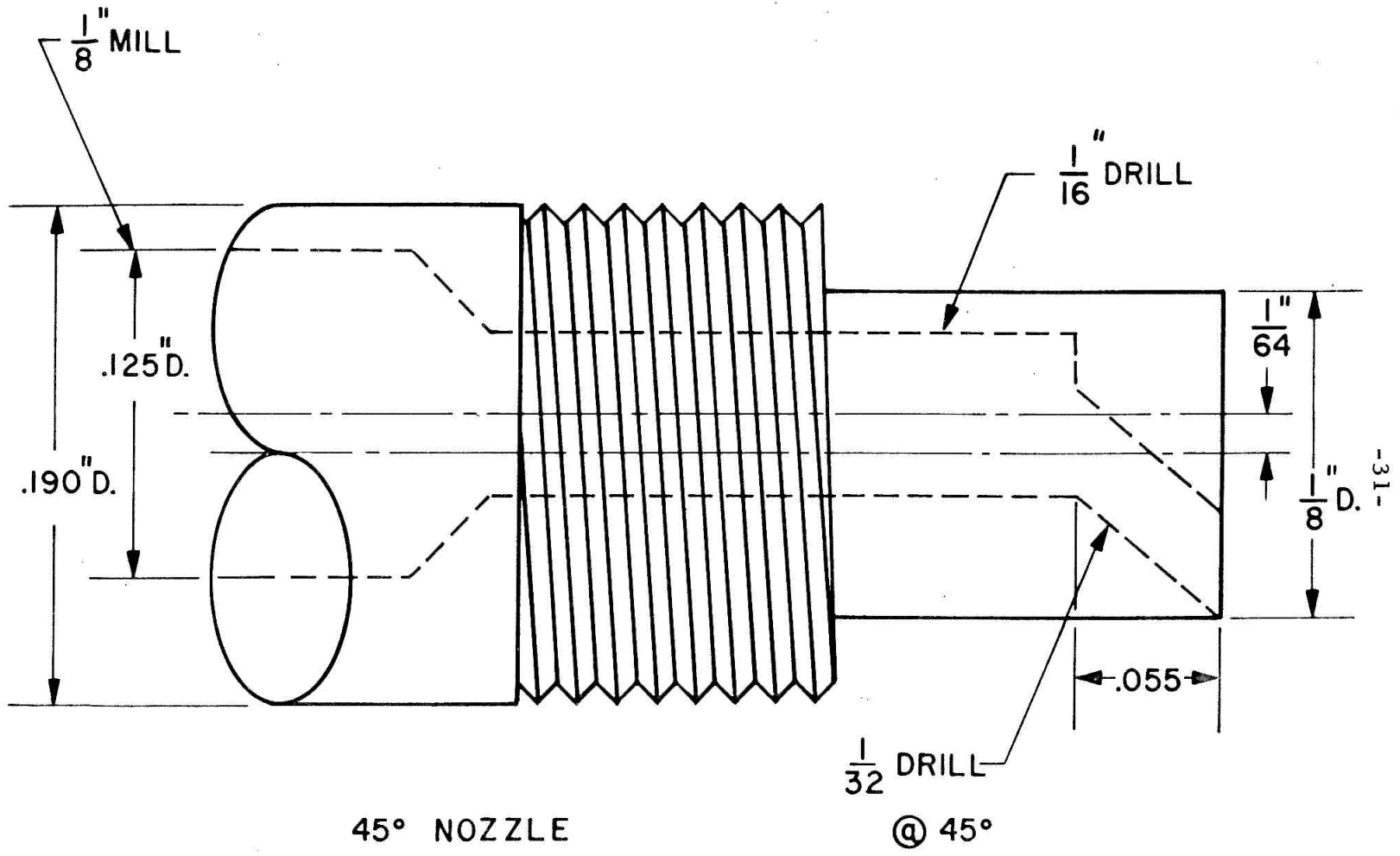
Fig. 1. Section View of the 45° Angle Nozzles.
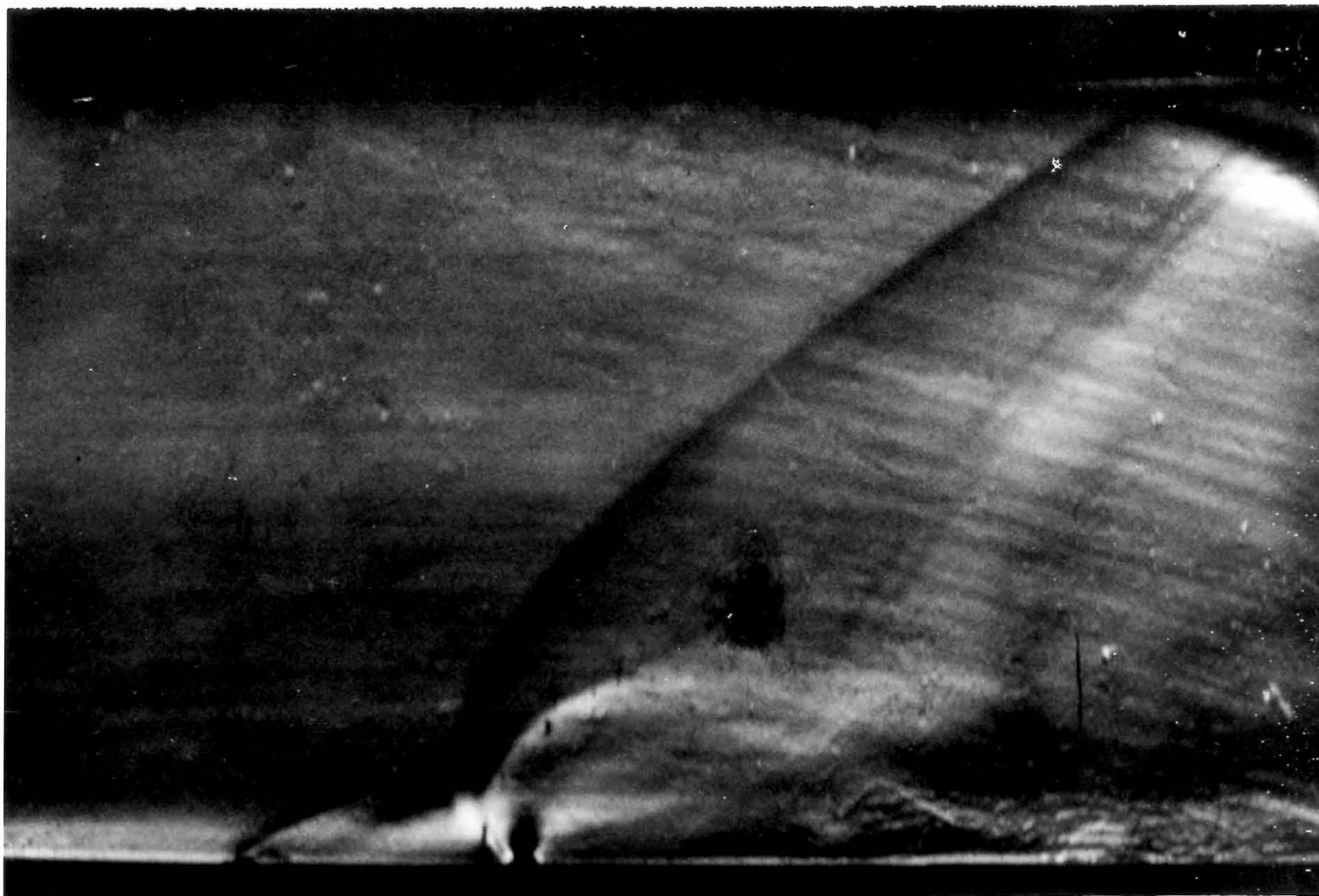
Fig. 2. Schlieren Photograph, Injection through Sonic Nozzle. Turbulent Boundary Layer, P_{o_j} = 400 psig.
(Scale: 1" = .435")
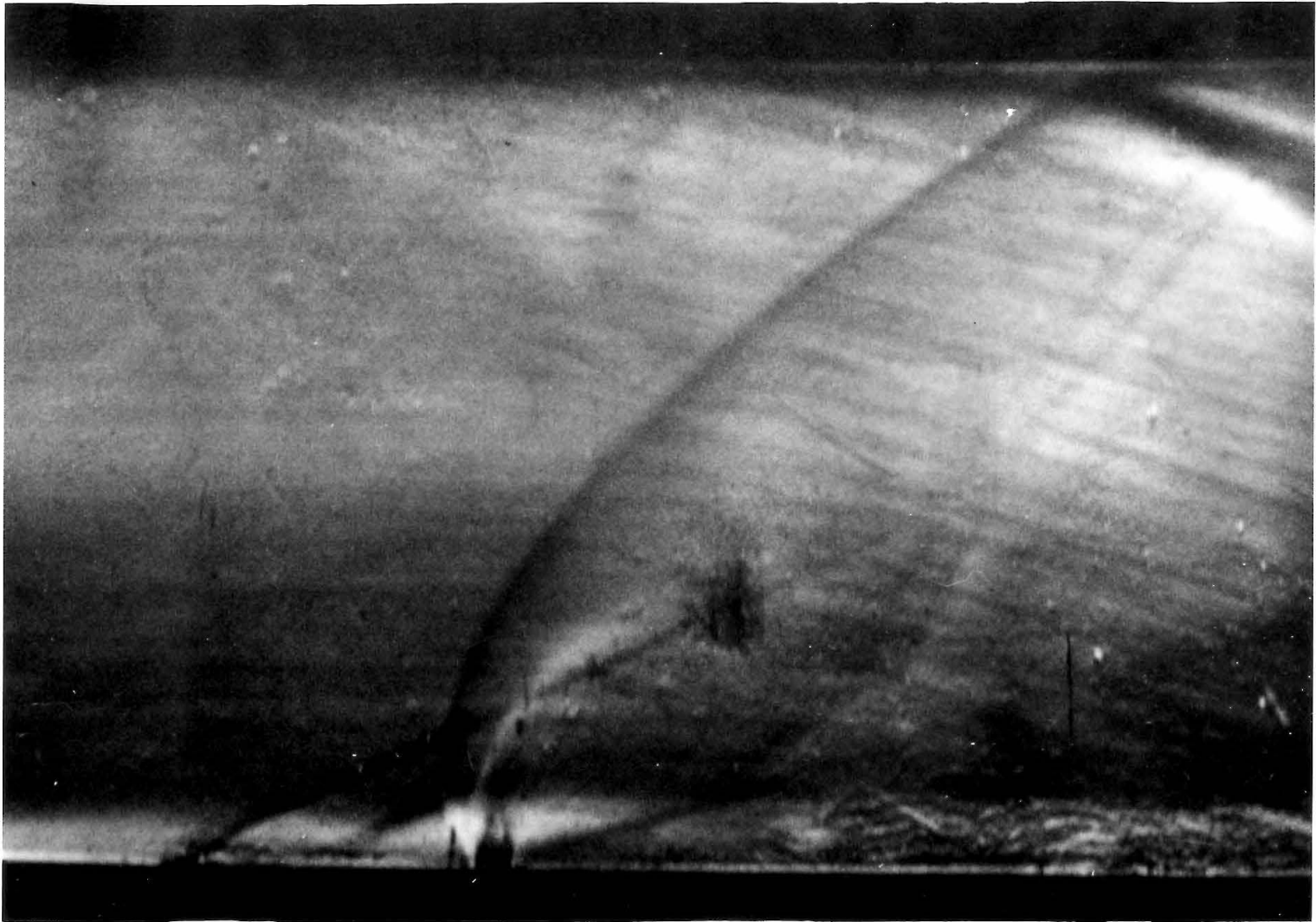
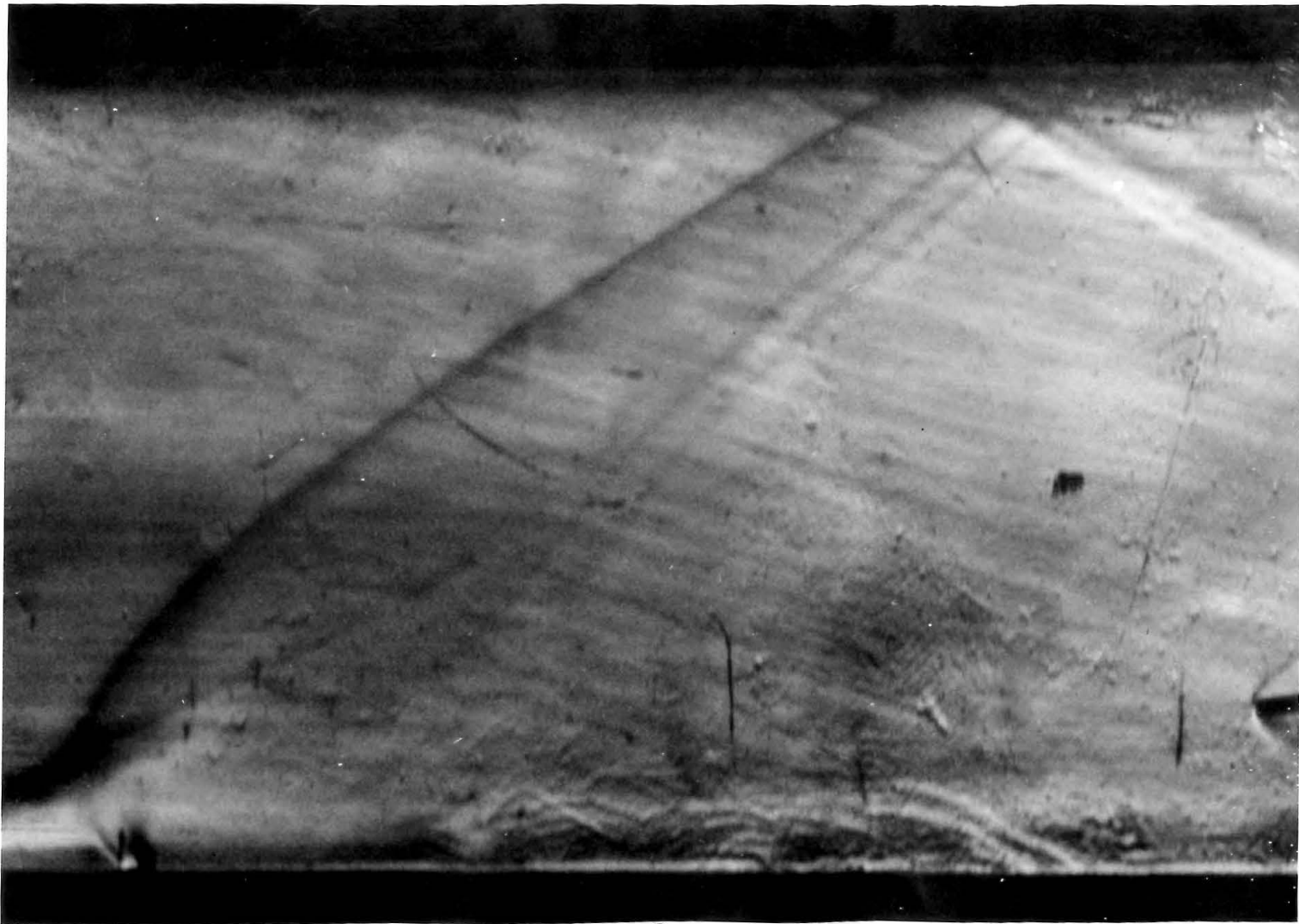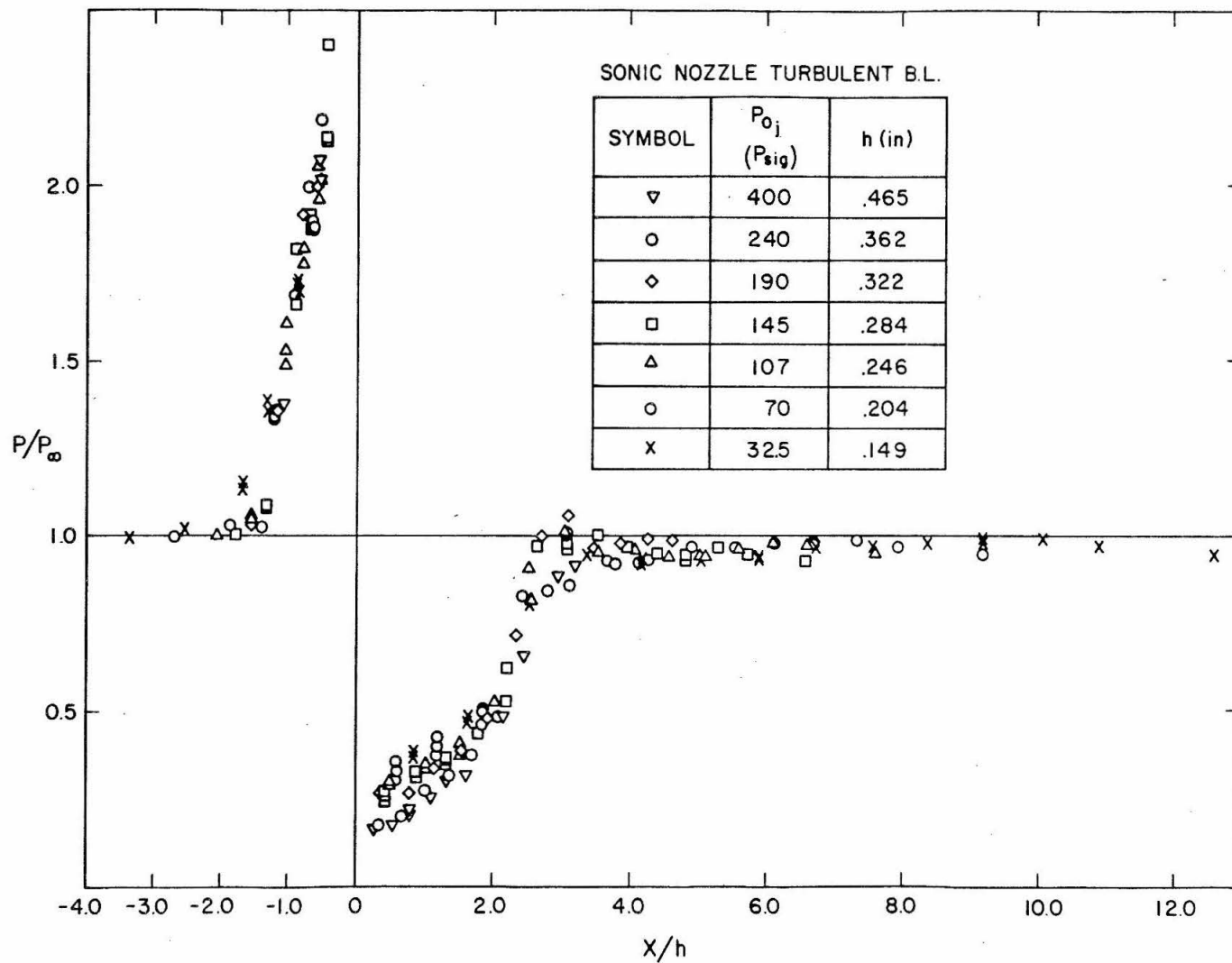Fig. 3. Schlieren Photograph, Injection through Supersonic Nozzle. Turbulent Boundary Layer, P_{o_j} = 400 psig. (Scale: $1'' = .435''$)
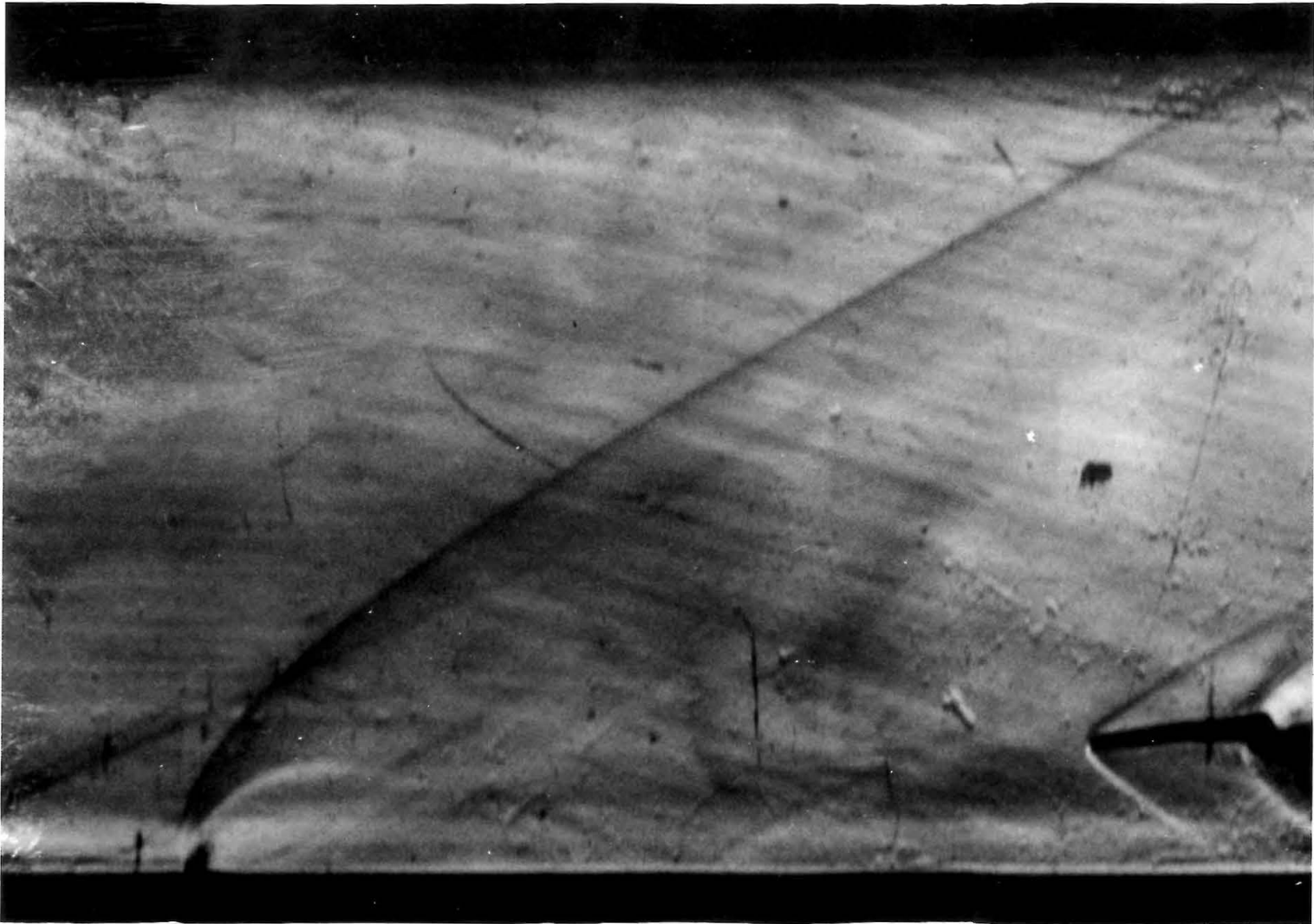
Fig. 4. Schlieren Photograph, Injection through 45° Downstream Nozzle. Turbulent Boundary Layer, P_{o_j} = 400 psig. (Scale: 1" = .435") (Four-Pronged Probe Shown on Right.)
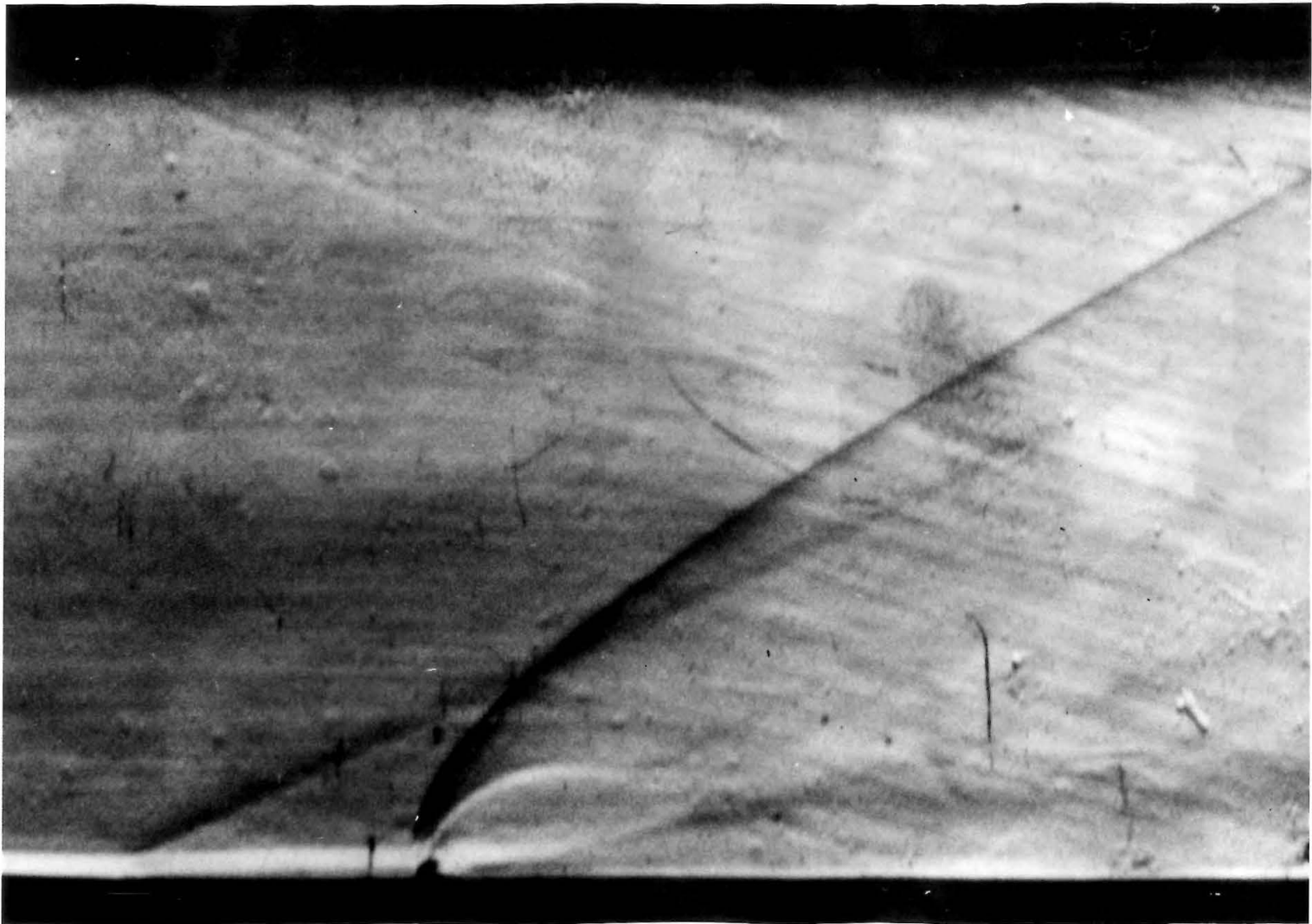
Fig. 5. Schlieren Photograph, Injection through 45° Downstream Nozzle. Laminar Boundary Layer, P_{O_j} = 400 psig. (Scale: $1'' = .435''$)

Fig. 6. Schlieren Photograph, Injection through 45° Upstream Nozzle. Turbulent Boundary Layer, P_{o_j} = 400 psig. (Scale: 1" = .435")

Fig. 7. Static Pressure Measurements on the Wall in the Plane y/h = 0. Sonic Nozzle, Turbulent Boundary Layer.
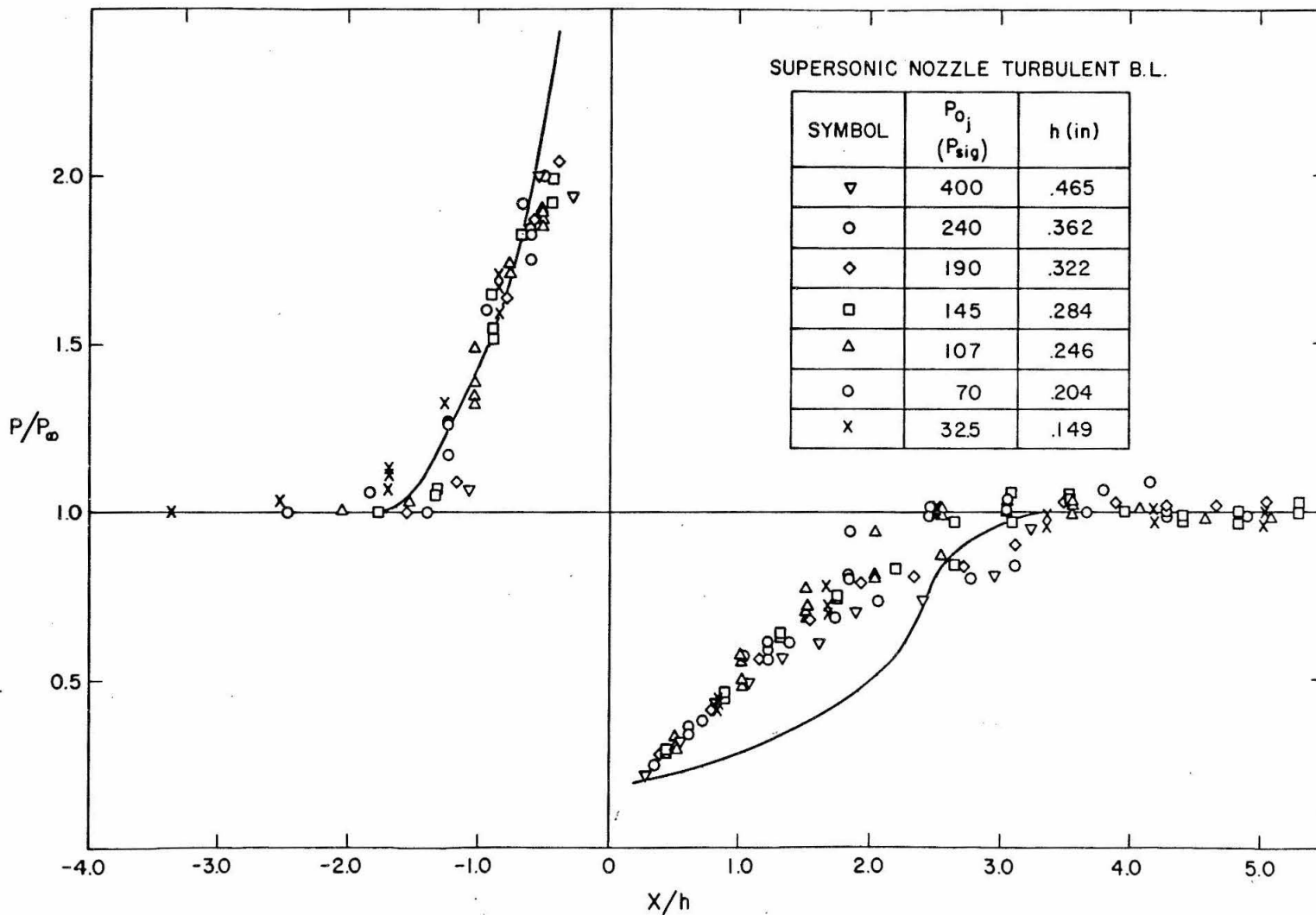
SUPERSONIC NOZZLE TURBULENT B.L.

SYMBOL	P_{o_j} (P$_{sig}$)	h (in)
▽	400	.465
○	240	.362
◇	190	.322
□	145	.284
△	107	.246
○	70	.204
✕	32.5	.149

Fig. 8. Static Pressure Measurements on the Wall in the Plane $y/h = 0$. Supersonic Nozzle, Turbulent Boundary Layer. (Solid Line Indicates Average of Sonic Nozzle Data for Comparison.)

45° NOZZLES (UPSTREAM and DOWNSTREAM) TURBULENT B.L.

P_{O_j} (P_sig)	SYMBOL U	SYMBOL D	h (in) U	h (in) D
400	▽	▼	.289	.226
240	◇	◆	.224	.176
190	○	●	.199	.157
145	□	■	.176	.138
107	△	▲	.152	.121
70	○	●	.126	.099
32.5	NONE	X	.092	.072

P/P_∞

3.0

2.0

1.0

-3   -2   -1.0   0   1.0   2.0   3.0   4.0   5.0   6.0   7.0   8.0   9.0   10.0

X/h

-39-
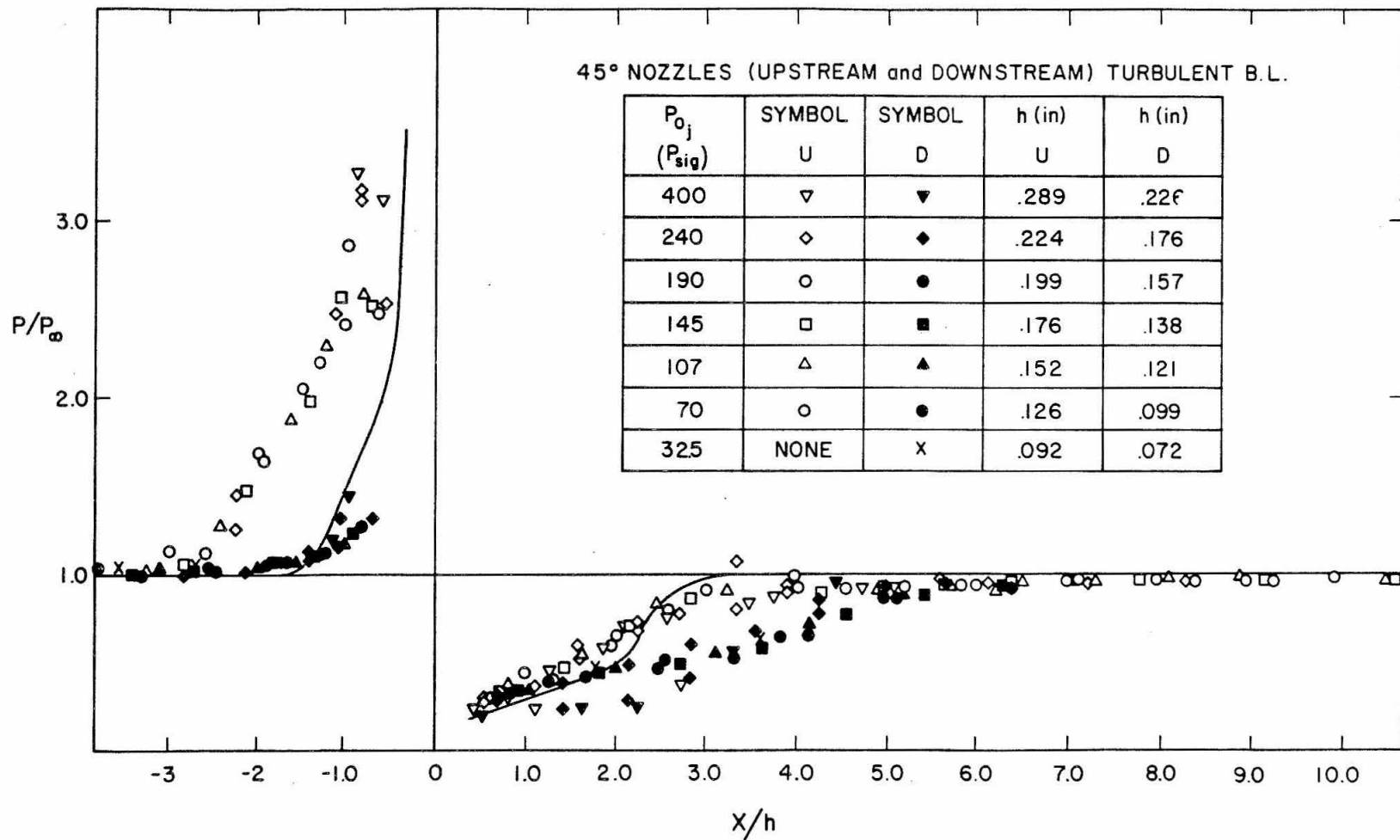
Fig. 9. Static Pressure Measurements on the Wall, in the Plane y/h = 0. 45° Upstream and Down-stream Nozzles, Turbulent Boundary Layer (Solid Line Indicates Average of Sonic Nozzle Data for Comparison).
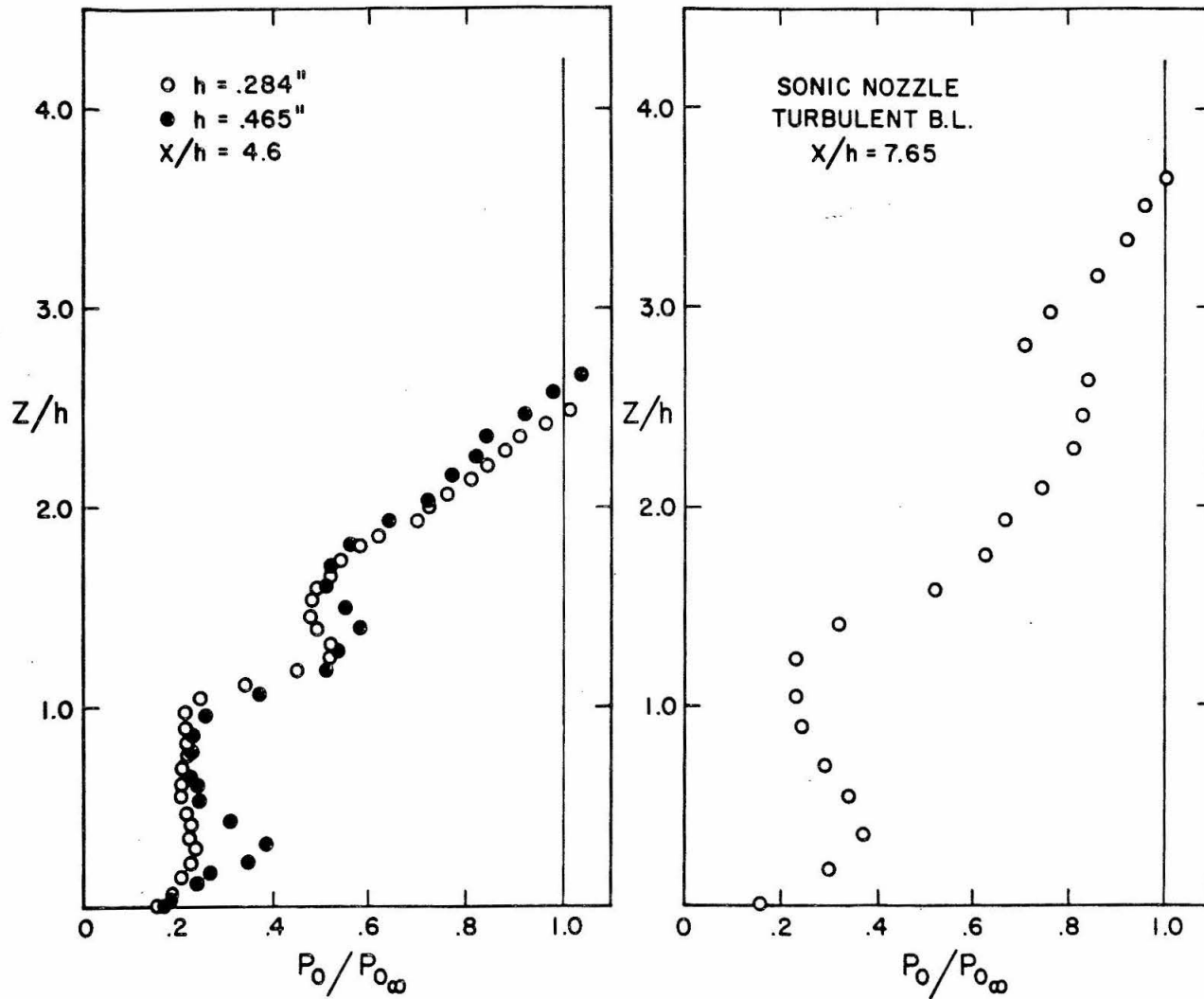
Fig. 10.   Total Pressure Profile in the Plane y/h = 0.   Sonic Nozzle, Turbulent Boundary Layer.
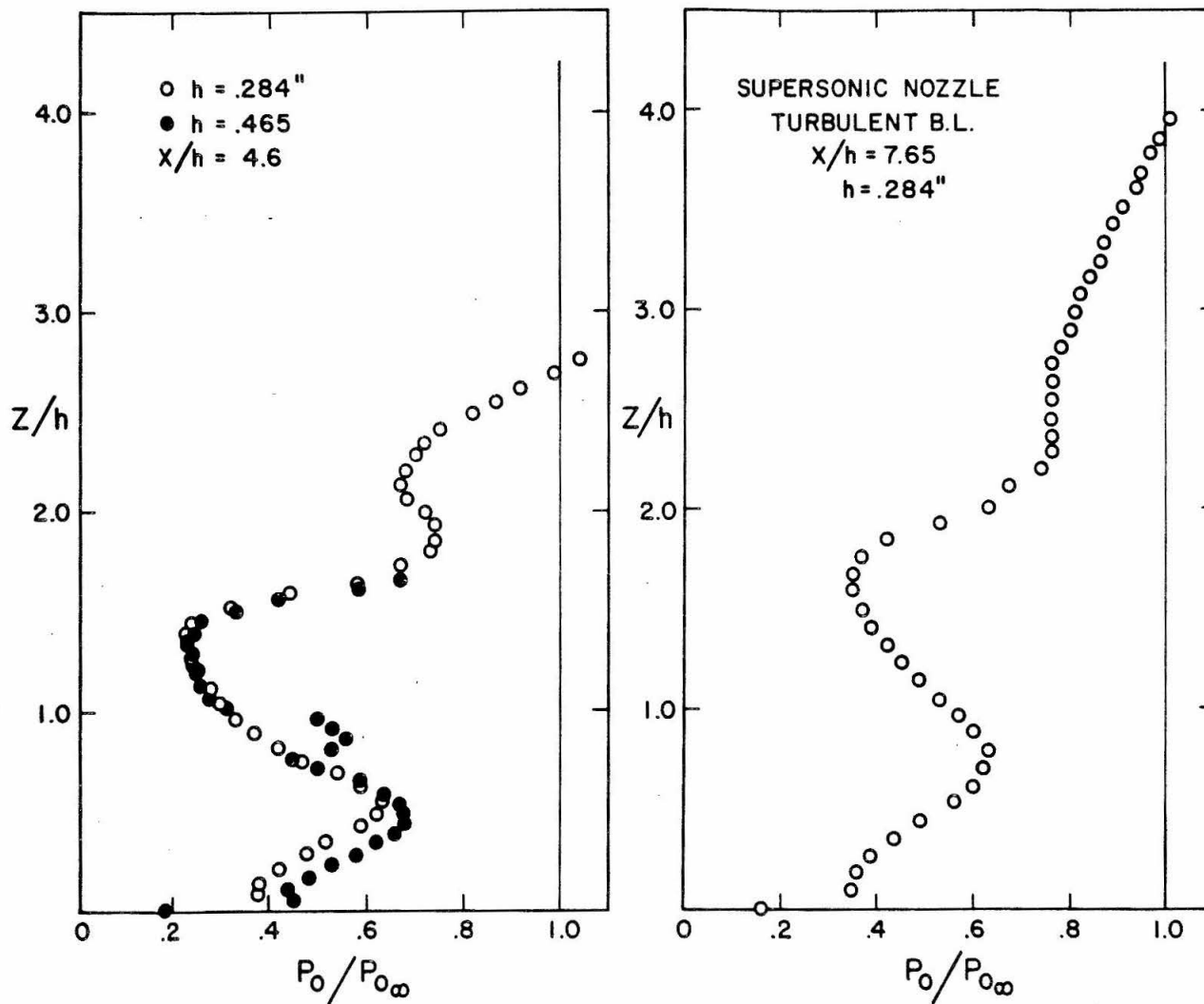
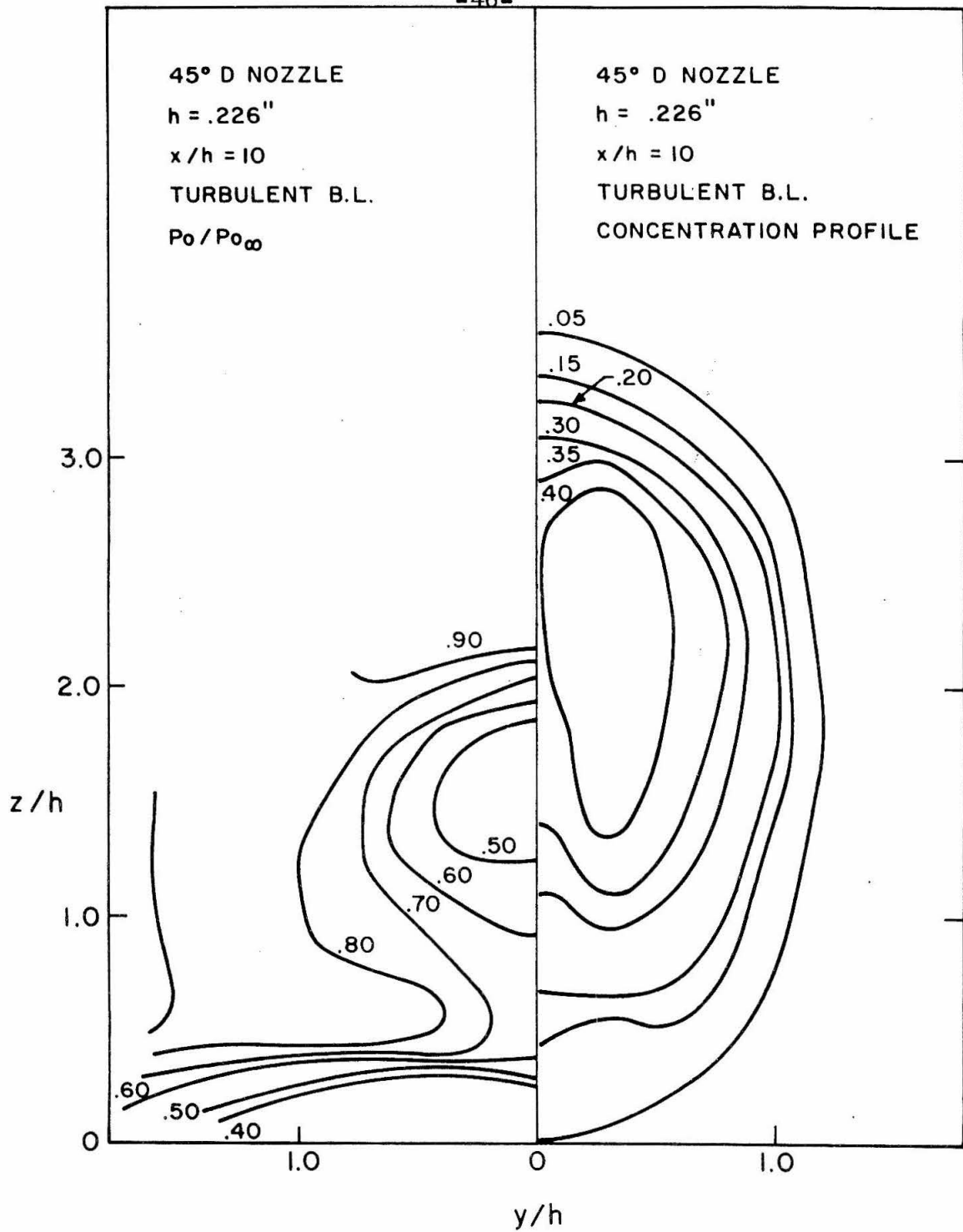Fig. 11. Total Pressure Profile in the Plane y/h = 0. Supersonic Nozzle, Turbulent Boundary Layer.
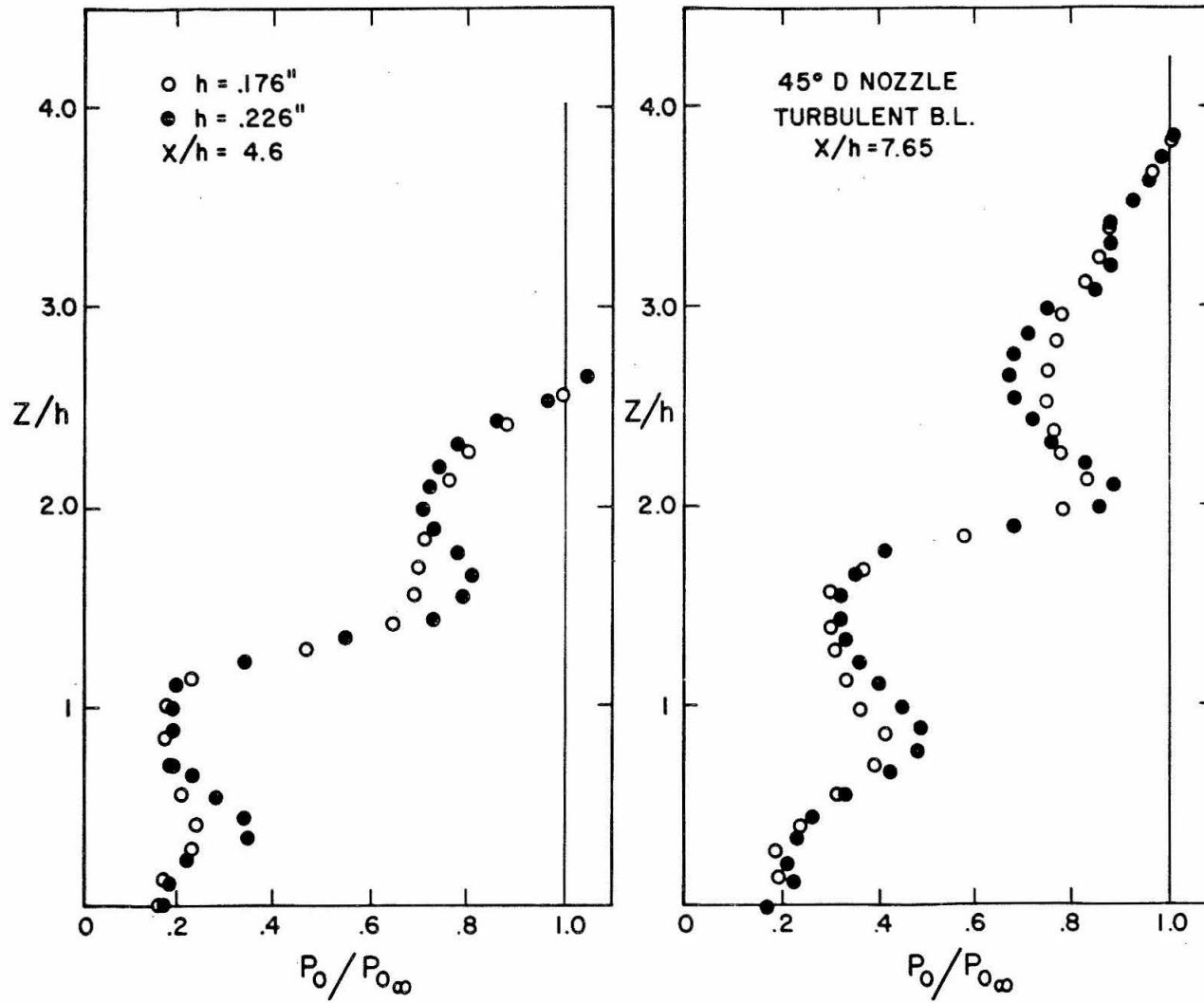
Fig. 12. Total Pressure Profile in the Plane y/h = 0. 45° Downstream Nozzle, Turbulent Boundary Layer.
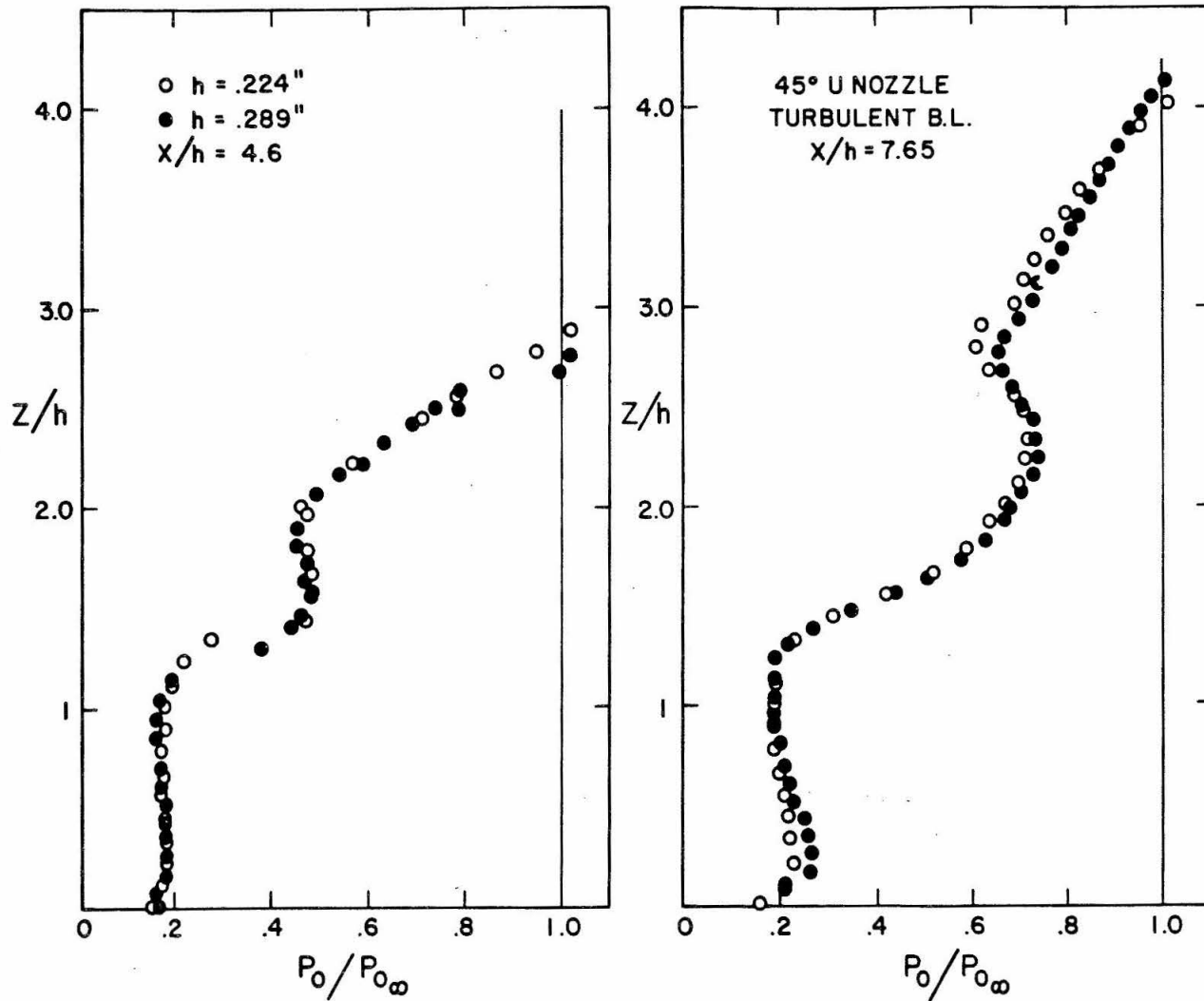
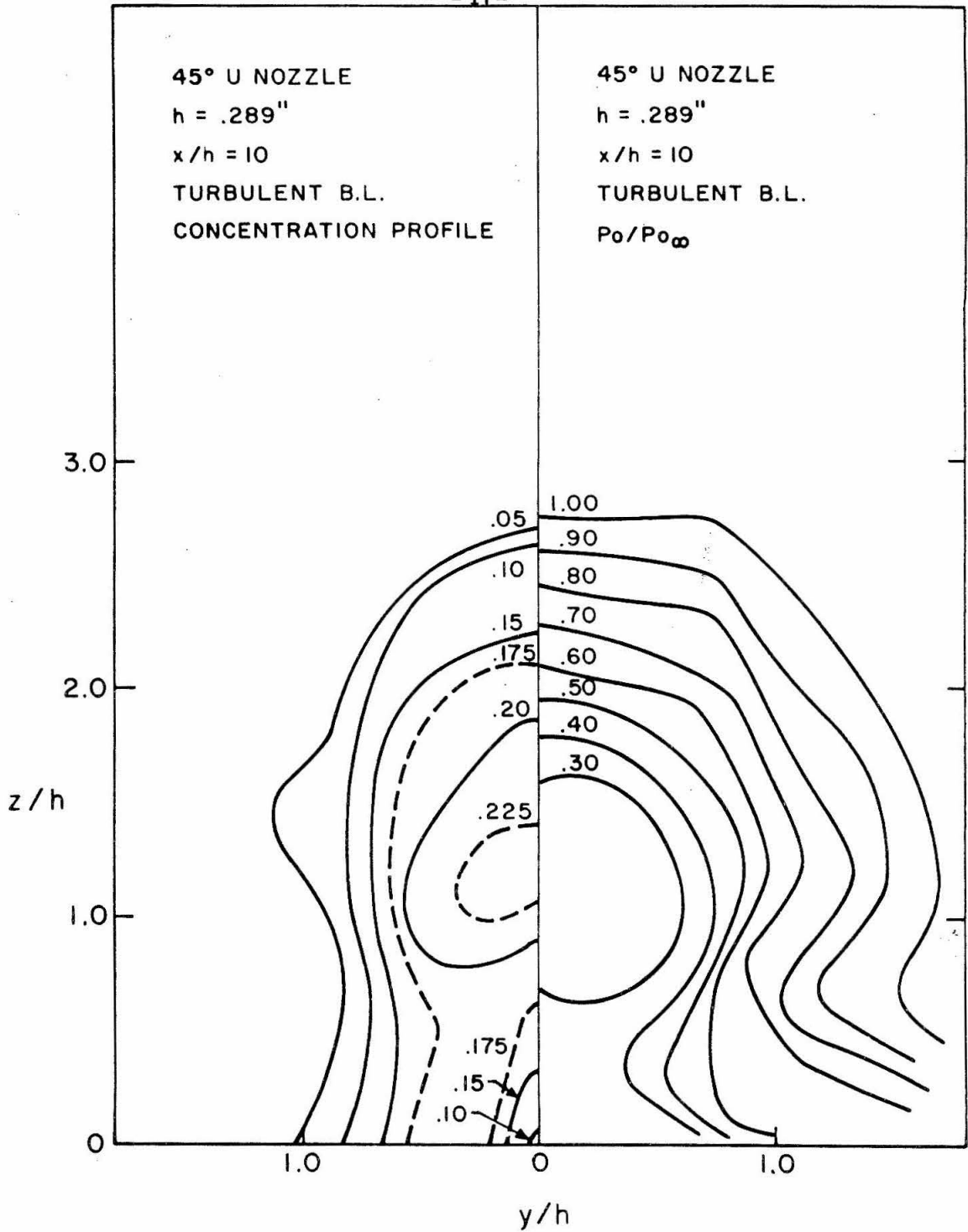Fig. 13. Total Pressure Profile in the Plane y/h = 0. 45° Upstream Nozzle, Turbulent Boundary Layer.
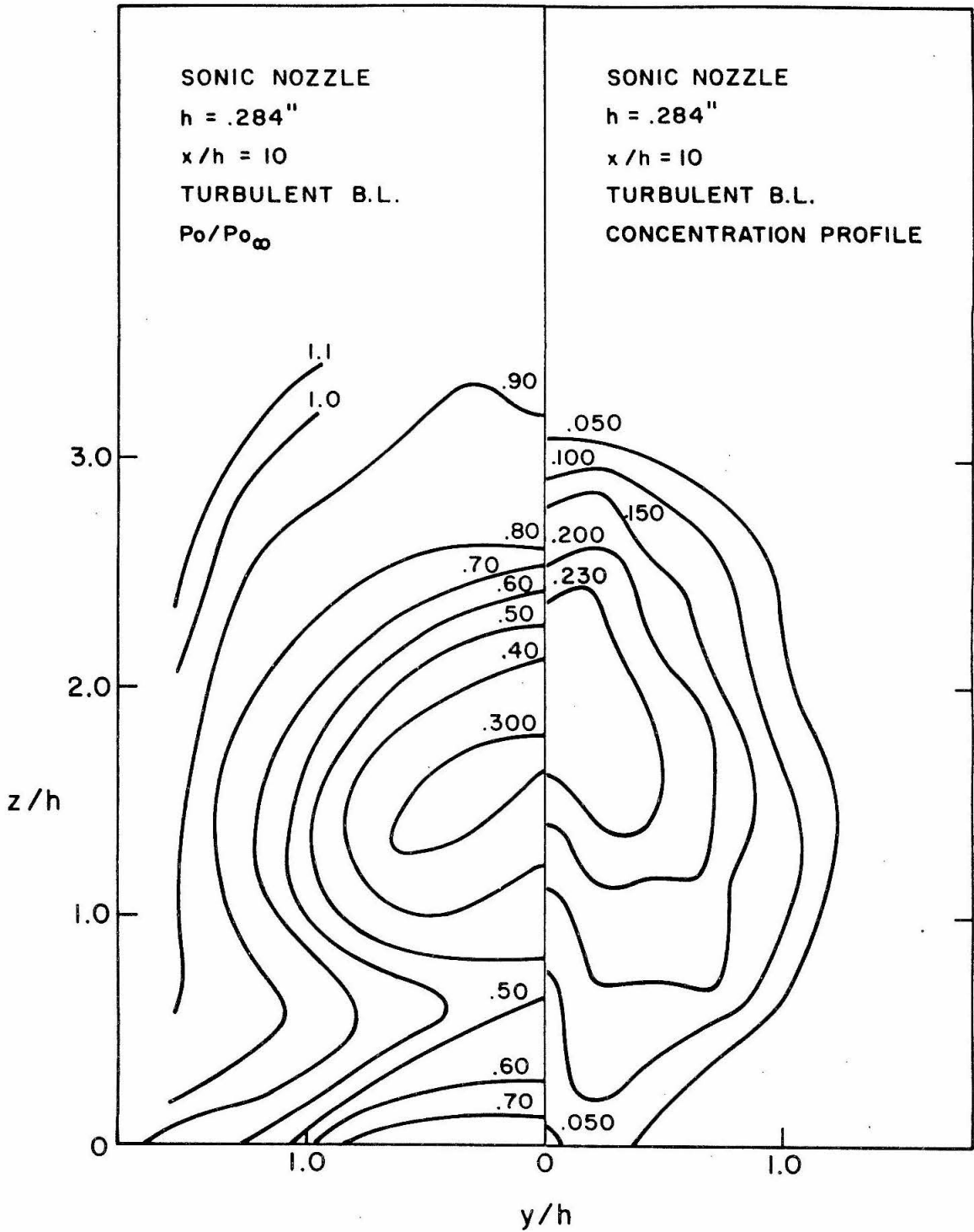
Fig. 14. Concentration and Total Pressure Contours in the Plane
x/h = 10. Sonic Nozzle, Turbulent Boundary Layer.
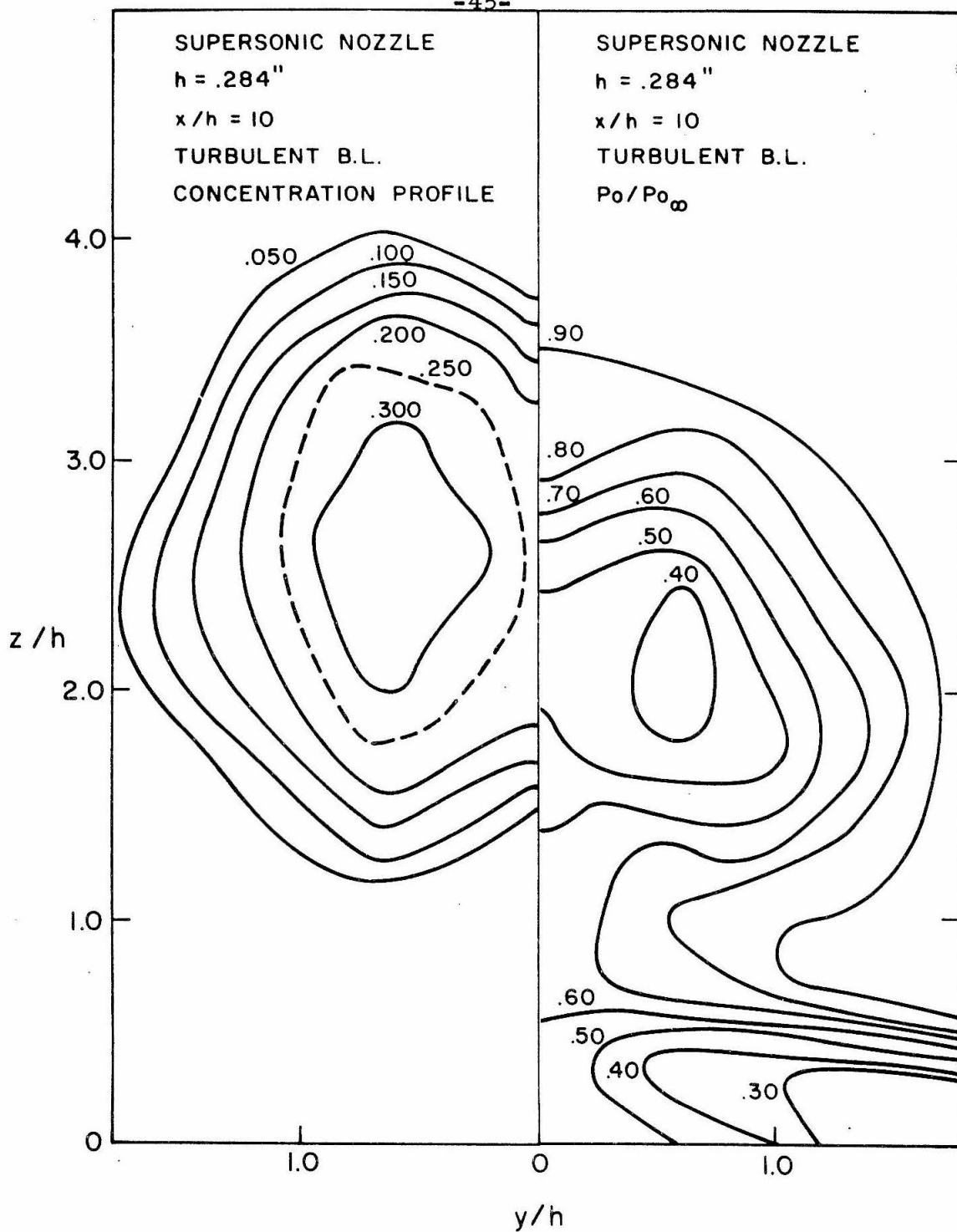
Fig. 15. Concentration and Total Pressure Contours in the Plane
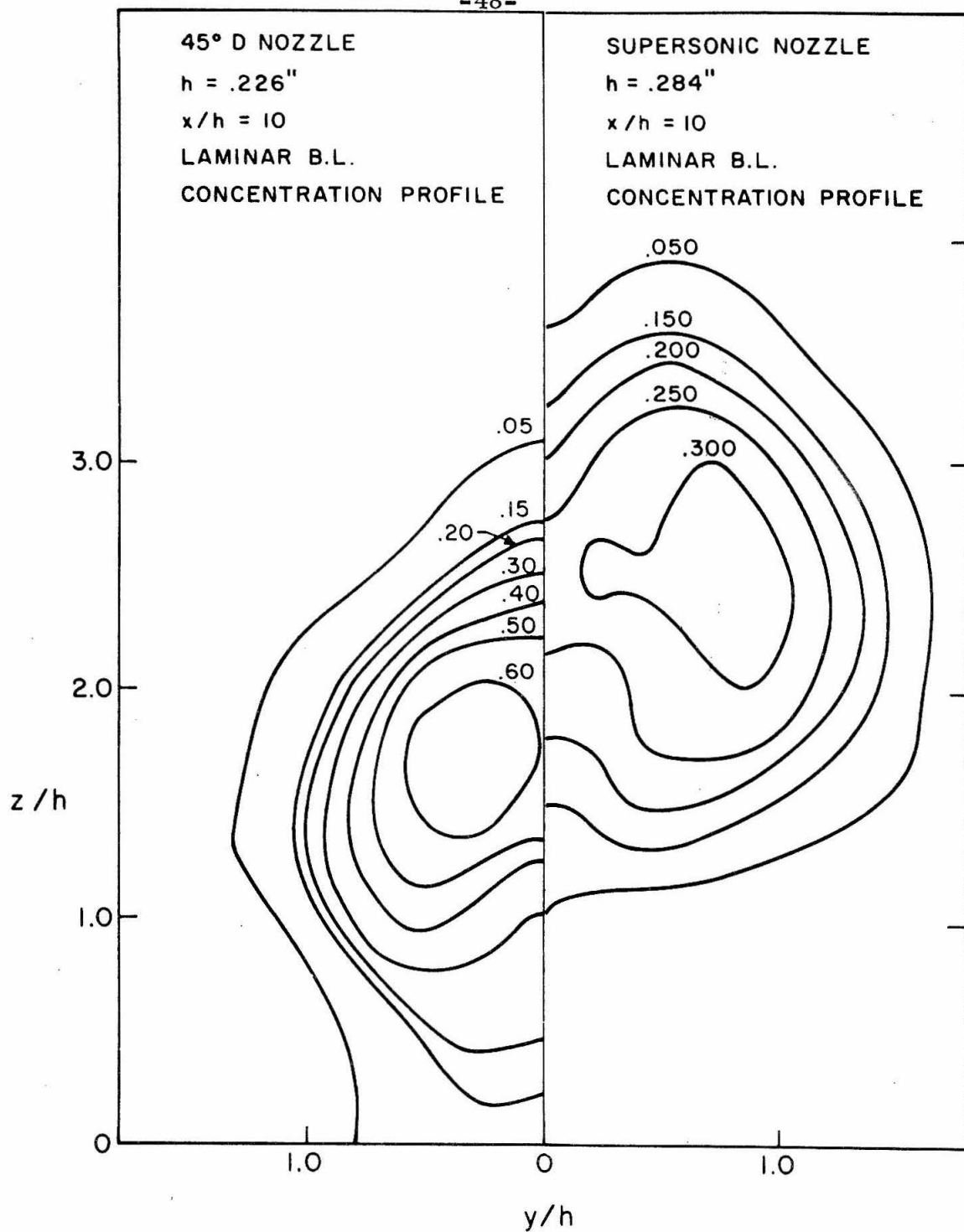x/h = 10. Supersonic Nozzle, Turbulent Boundary Layer.

Fig. 16. Concentration and Total Pressure Contours in the Plane
x/h = 10.   45° Downstream Nozzle, Turbulent Boundary Layer.

Fig. 17. Concentration and Total Pressure Contours in the Plane
x/h = 10. 45° Upstream Nozzle, Turbulent Boundary
Layer.

Fig. 18. Concentration Contours in the Plane x/h = 10. Supersonic and 45° Downstream Nozzles. Laminar Boundary Layer.
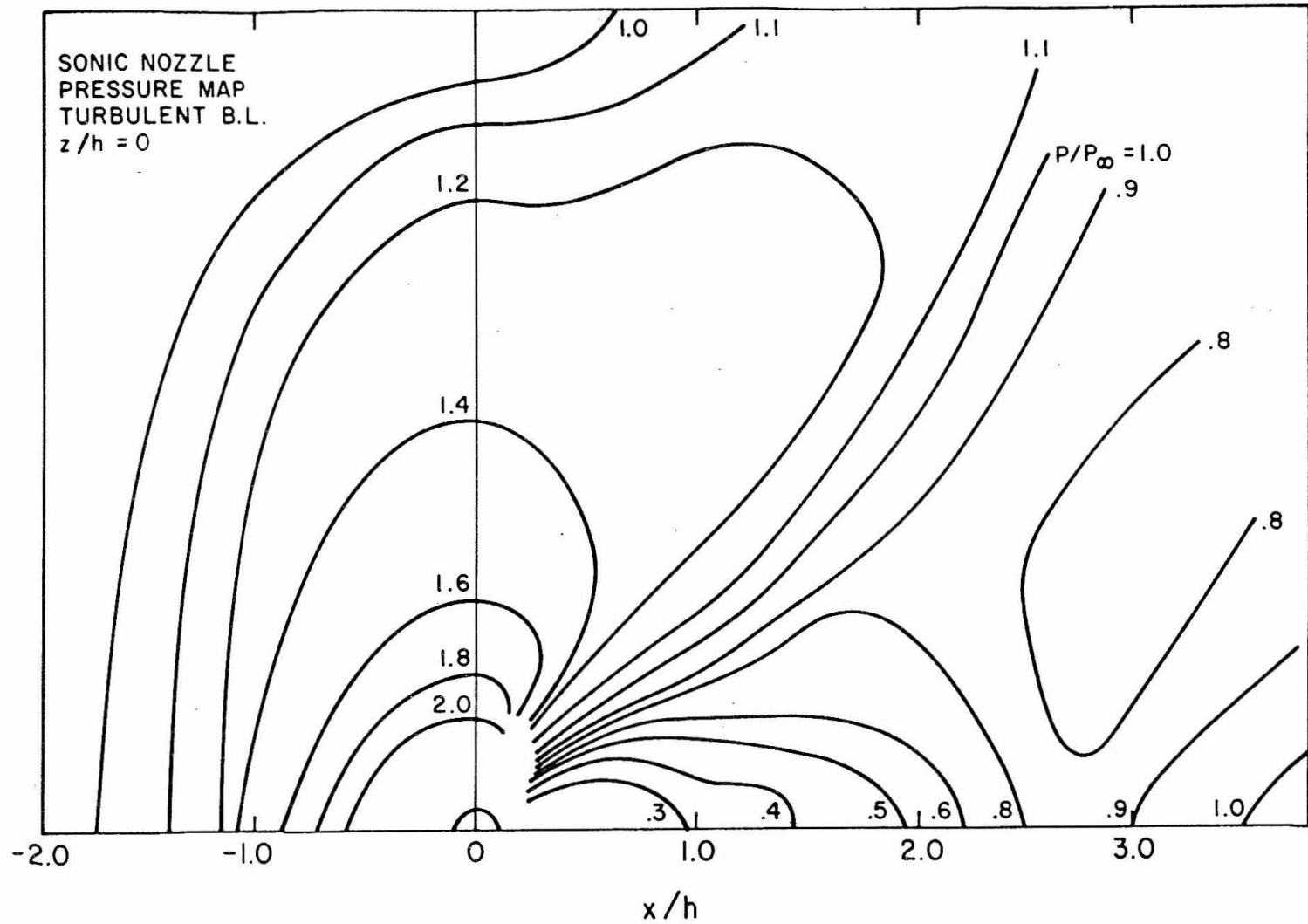
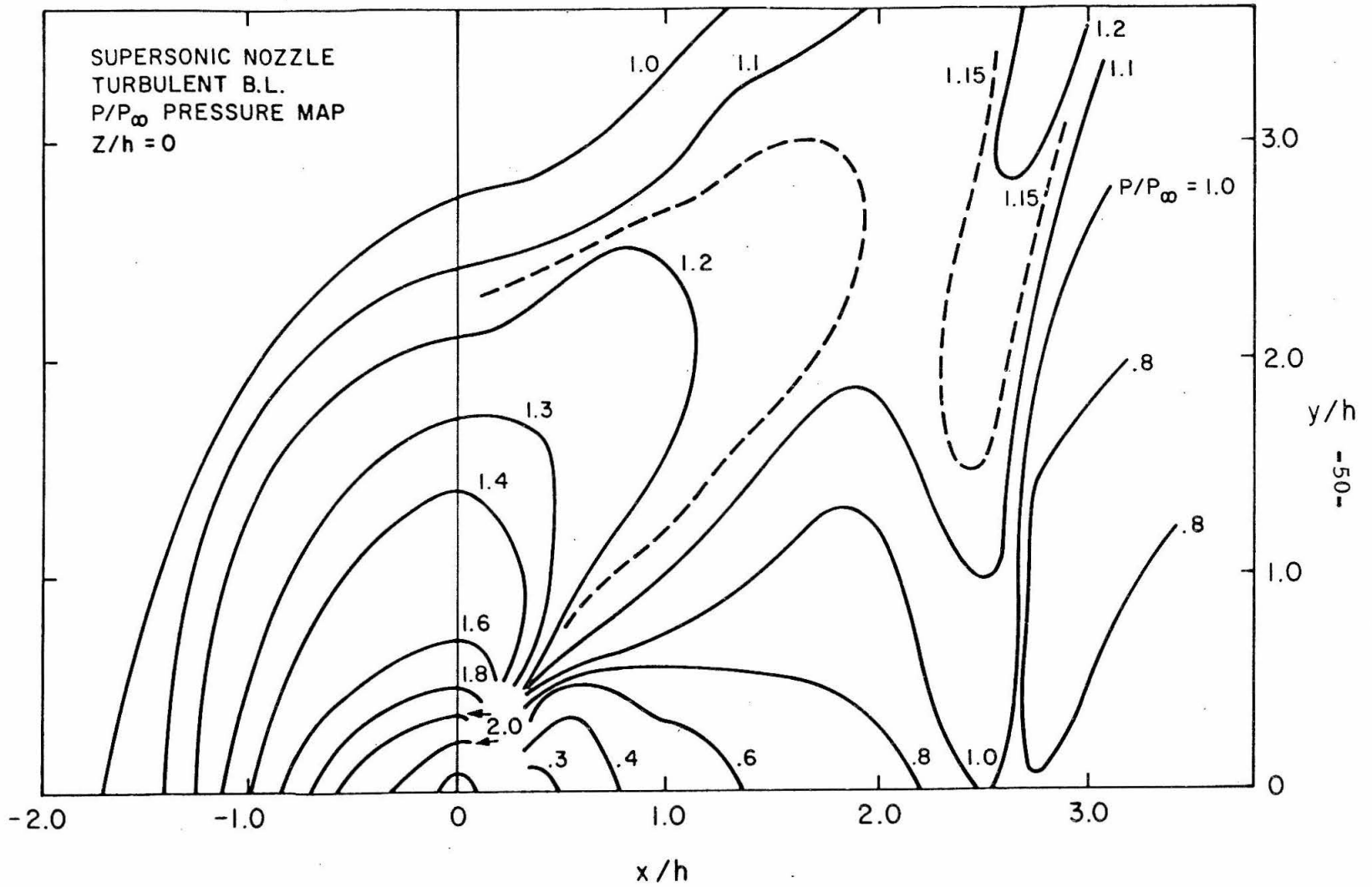Fig. 19. Wall Static Pressure Contour Map. Sonic Nozzle, Turbulent Boundary Layer.

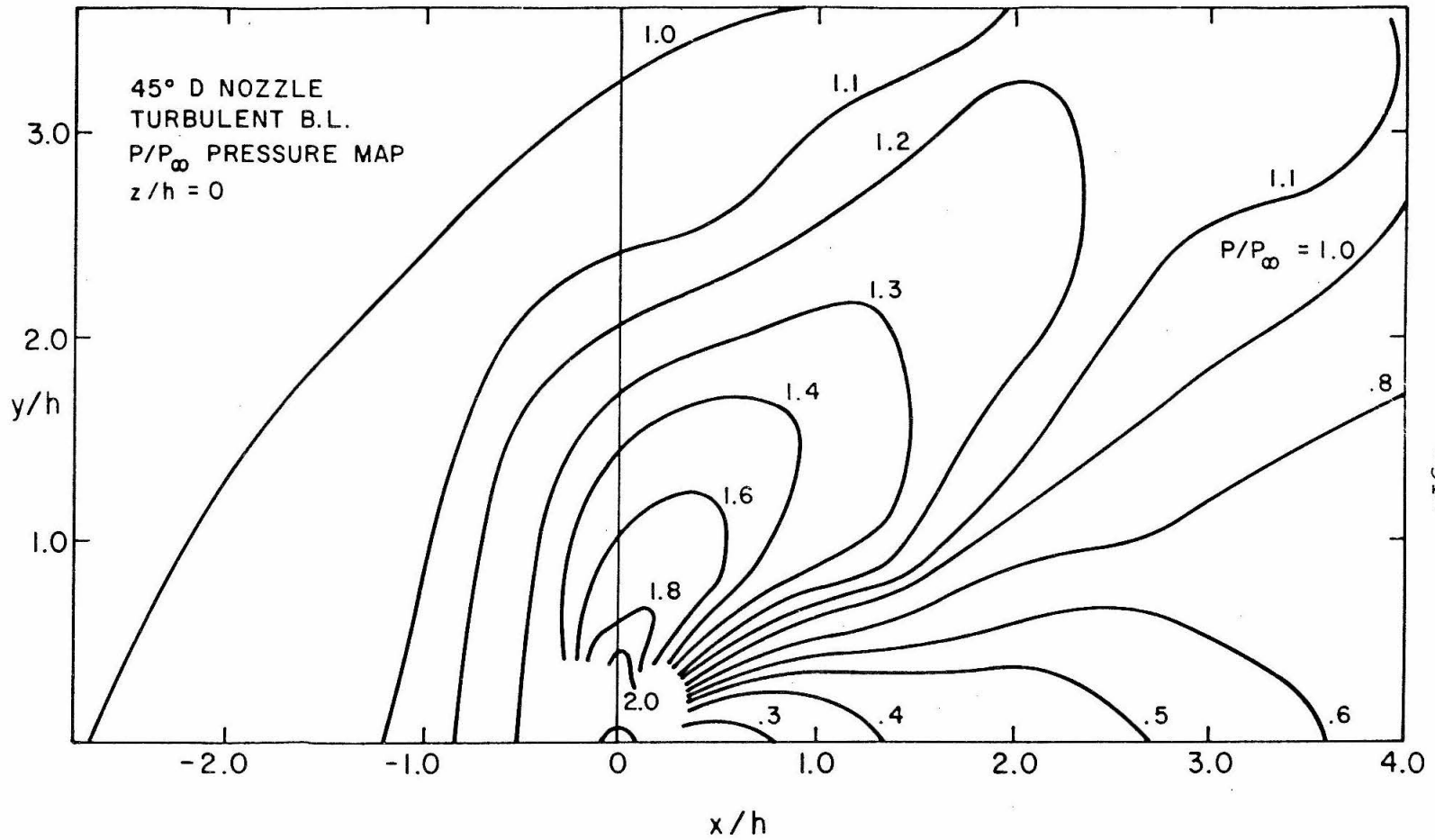Fig. 20. Wall Static Pressure Map. Supersonic Nozzle, Turbulent Boundary Layer.

Fig. 21. Wall Static Pressure Map. 45° Downstream Nozzle, Turbulent Boundary Layer.
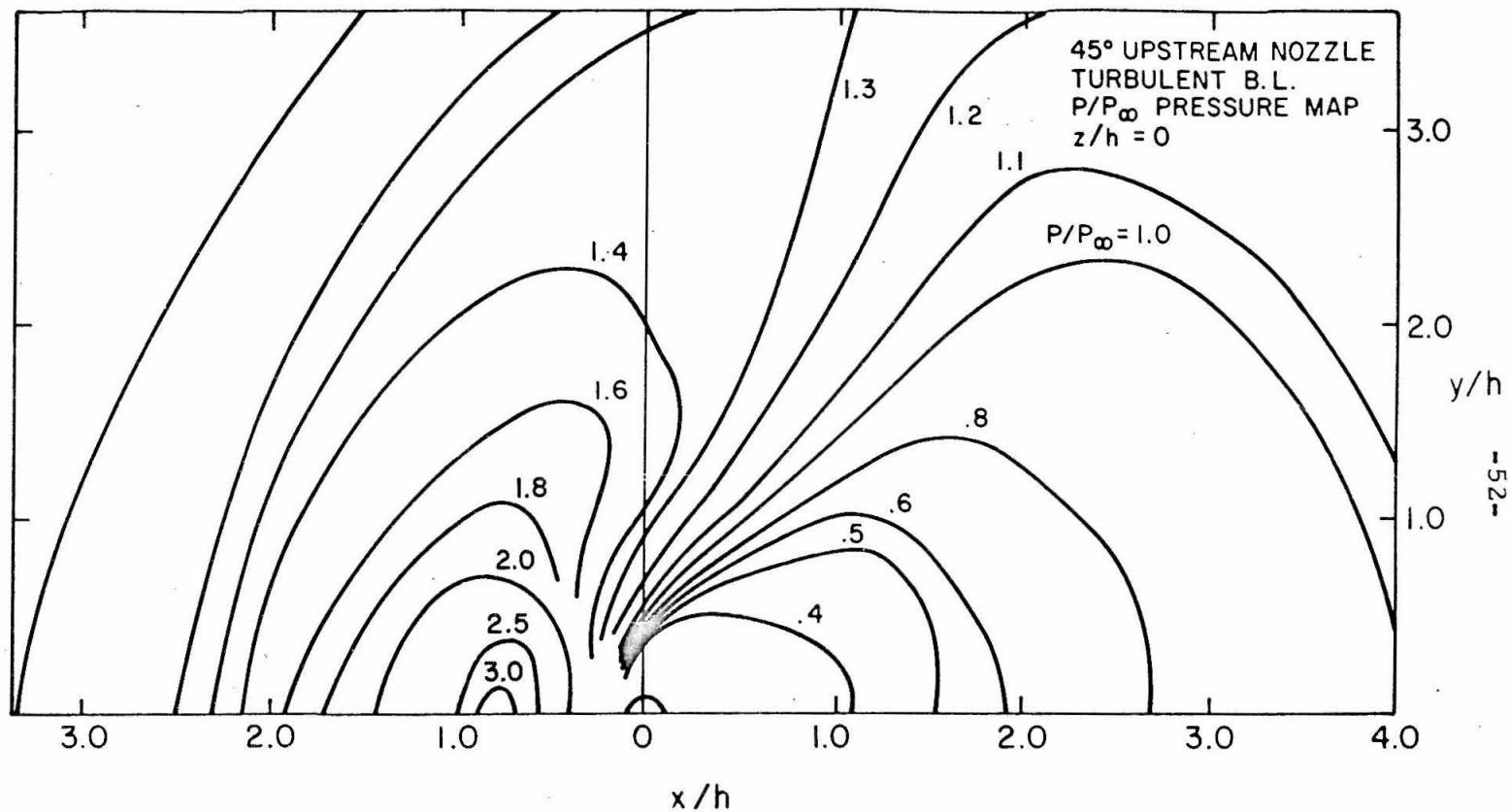
Fig. 22.   Wall Static Pressure Map.   45° Upstream Nozzle, Turbulent Boundary Layer.